HAL
open science

Synthesis, structural characterization, antibacterial activity, DFT computational studies and thermal analysis of two new thiocyanate compounds based on 1-phenylpiperazine

Chaima Gharbi, Baya Toumi, Sarra Soudani, Frédéric Lefebvre, Werner Kaminsky, Christian Jelsch, Chérif Ben Nasr, Lamia Khedhiri

To cite this version:

Chaima Gharbi, Baya Toumi, Sarra Soudani, Frédéric Lefebvre, Werner Kaminsky, et al.. Synthesis, structural characterization, antibacterial activity, DFT computational studies and thermal analysis of two new thiocyanate compounds based on 1-phenylpiperazine. Journal of Molecular Structure, 2022, 1257, pp.132620. 10.1016/j.molstruc.2022.132620 . hal-03584972

HAL Id: hal-03584972

https://hal.science/hal-03584972v1

Submitted on 22 Feb 2022

HAL is a multi-disciplinary open access archive for the deposit and dissemination of scientific research documents, whether they are published or not. The documents may come from teaching and research institutions in France or abroad, or from public or private research centers.

L'archive ouverte pluridisciplinaire **HAL**, est destinée au dépôt et à la diffusion de documents scientifiques de niveau recherche, publiés ou non, émanant des établissements d'enseignement et de recherche français ou étrangers, des laboratoires publics ou privés.

Published in *Journal of Molecular Structure*, 2022, 132620.
10.1016/j.molstruc.2022.132620

Synthesis, structural characterization, antibacterial activity, DFT computational studies and thermal analysis of two new thiocyanate compounds based on 1-phenylpiperazine

Chaima Gharbi[1], Baya Toumi[2], Sarra Soudani[1], Frédéric Lefebvre[3], Werner Kaminsky[4], Christian Jelsch[5], Chérif Ben Nasr[1], Lamia Khedhiri[6,*]

[1] Laboratoire de Chimie des Matériaux, Université de Carthage, Faculté des Sciences de Bizerte, 7021 Zarzouna, Tunisie.

[2] Laboratoire Matériaux Traitement et Analyse (LMTA), Institut National de Recherche et d'Analyse physico-chimique (INRAP), Sidi Thabet, 2020 Ariana, Tunisie

[3] Laboratoire de Chimie Organométallique de Surface (LCOMS), Ecole Supérieure de Chimie Physique Electronique, 69626 Villeurbanne Cedex, France.

[4] Department of Chemistry, University of Washington, 98105 Seattle, Washington, USA.

[5] Institut Jean Barriol, Université de Lorraine, CNRS, CRM2, F-54000 Nancy, France

[6] Laboratoire des Matériaux Utiles (LMU), Institut National de Recherche et d'Analyse physico-chimique (INRAP), Sidi Thabet, 2020 Ariana, Tunisie

[*] Corresponding author: Lamia Khedhiri (lkhedhiri.loulou@yahoo.com)

Abstract:

Two hybrid materials, $(HPhPip)_2[Co(NCS)_4]$ (I) and (HPhPip)(NCS)·PhPip (II), were grown using the slow evaporation method. The characterization of both compounds was accomplished by means of different analytical techniques such as IR, TGA–DTA, and single X-ray diffraction. XRD showed that compounds (I) and (II) crystallized into triclinic and noncentrosymmetric orthorhombic systems, respectively. In Compound (I), the Co (II) ion is

surrounded by four NCS^- anions and shows a distorted tetrahedral coordination geometry. Crystal packing analysis indicates that the $[Co(NCS)_4]^{2-}$ anion and 1-phenylpiperazinium cation are linked together through N–H…S to form a graph set. Compound (II) presents an interesting 3-D network via N–H…N, C–H…S, and C–H⋯π intermolecular interactions between $HPhPip^+$, NCS^-, and PhPip, consolidating the stacking of the crystal. FT-IR was used to explore the modes of vibration of the different functional groups present in two compounds. A theoretical investigation has also been performed via DFT on the molecular structure of compounds, allowing the determination of the Mulliken charge distribution, the Molecular Electrostatic Potential maps, and the HOMO–LUMO diagrams. The Hirshfeld surface, two-dimensional fingerprint plots and enrichment ratio were investigated to indicate the important role of intermolecular interactions. The robust thermal stability of the two crystals was ensured by thermogravimetric–differential thermal analysis. Finally, the bacterial potency of two compounds has been surveyed.

Keywords: thiocyanate precursor; cobalt(II) complex; crystal structure; IR; Hirshfeld surface; contact enrichment ratio; DFT calculations; thermal analysis; antibacterial activity

1. Introduction

Over the past decades, the main capacity of transition metals attracted great attention due to their promising properties and their capability of performing versatile covalent bonds [1–4]. Cobalt coordination complexes exhibit intriguing properties that make them suitable for a remarkable breadth of tremendous potential applications in functional materials, for instance, catalysis, fluorescent, magnetic storage, and biomedical [5–14]. Additionally, these compounds can theoretically be harnessed in the preparation of systems that modulate biological functions [15]. Most importantly, cobalt has a number of possible oxidation states (Co^+, Co^{2+}, Co^{3+}, and Co^{4+}) [16]. The Co(II) complexes exhibit relatively strong coordinating abilities and diverse

geometries, which depend on the crystal packing. The coordination numbers can be four [17] (tetrahedral), five [18] (square pyramidal geometries), and six (octahedral geometry) [19].

In recent years, significant efforts dealing with pseudo-halides especially of the thiocyanate-possessing versatile bonding modes have been reported owing to their outstanding properties in many fields. As it is ambidentate, the thiocyanate anion is an appropriate candidate for developing building blocks assembling coordination chemistry, leading to the formation of complexes with multidimensionality and diversified structures [20–22]. In fact, the thiocyanate anion is a bidentate ligand, which has numerous terminals and bridging coordination modes with two donor atoms either by sulfur or by nitrogen [23]. Thus, the flexible coordination features of these anions could stabilize the intermediate states of the transition metal centers inducing varied crystal structures.

The formation of complexes between organic molecules and cobalt–isothiocyanate moieties is especially important for their use in diverse fields of technological applications [24,25]. In view of the importance of piperazines the structural chemistry of various compounds that include piperazine and its derivatives does not cease to develop and continues to be a subject of research in many laboratories [26–36]. Piperazine and its derivatives have plentiful potential applications and are important ligands for constructing coordination complexes. Specifically, piperazine has been examined as an intercalator in recent years thanks to its promising biological activities in the assembly of organic–inorganic hybrid materials [37–41]. Accordingly, recent statistical studies have shown that piperazine is the third most commonly used N-heterocyclic system behind piperidine and pyridine in pharmaceutical fields [42,43]. Mostly, piperazine derivatives have been extensively studied in the field of medicinal chemistry due to their multivalent biological profile. A large number of therapeutic activities such as antimicrobial [44], analgesic [45], anticonvulsant [46], antitumor [47], antimalarial [48], and antiviral [49] activities have been displayed by compounds adjoining this heterocyclic system.

As a continuation of our contribution in developing the successful synthesis of new coordination compounds containing the same ligand, we have investigated the effect of incorporation of the transition metal on crystallographic characteristics, surface morphology, thermal stability, and biological properties; here, we report a detailed structural study, Hirshfeld surface analysis, IR spectroscopic characterization, thermal behavior, and biological potential of $(HPhPip)_2[Co(NCS)_4]$ (I) and (HPhPip)(NCS)·PhPip (II). The noncovalent intermolecular contacts, such as electrostatic, Van der Waals and hydrogen bonding interactions, are presented in these compounds, and their effects on the overall architectures are discussed in detail.

2. Experimental

2.1. Chemical Preparation

2.1.1. Materials

All chemicals were obtained from commercial sources and used as received.

2.1.2. Preparation of $(HPhPip)_2[Co(NCS)_4]$ (I)

The solution mixture resulted from the addition of anhydrous $CoCl_2$ (129.84 mg, 1 mmol) and KSCN (388.72 mg, 4 mmol) in 15 mL of water was stirred for 2 h at room temperature. A solution of 1-phenylpiperazine (324.46 mg, 2 mmol) in ethanol (15 mL) was then added drop by drop at room temperature. The final solution was stirred and heated for 30 min at 80 °C. The solution was filtered and kept for slow evaporation over a few weeks at room temperature until the appearance of blue single crystals with good morphology. Yield = 86% *Anal.* Calc. C, 46.62; H, 4.86 ; N, 18.13%; Found. C, 46.72; H, 4.95; N, 18.17.

2.1.3. Preparation of (HPhPip)(NCS)·PhPip (II)

A solution of KSCN (97.18 mg, 1 mmol) in 20 mL of water was added slowly to a solution of 1-phenylpiperazine (324.46 mg, 2 mmol) in ethanol at room temperature. The mixture solution was stirred for 2 h and filtered off. After allowing standing at room temperature

for about 3 weeks, brown crystals suitable for X-ray structural diffraction analysis were obtained. Yield = 84%. *Anal.* Calc. C, 64.86; H, 7.56; N, 18.25%; Found. C, 65.82; H, 7.85; N, 18.32.

2.2. X-ray Crystallography

X-ray diffraction analyses of compounds (I) and (II) were performed. Suitable single crystals were chosen under an optical microscope. The intensity data of (I) were measured on a Bruker Smart APEX-II diffractometer equipped with a graphite monochromated employing MoKα radiation (λ = 0.71073 Å). X-ray diffraction measurements of (II) were carried out on a Nonius Kappa CCD diffractometer containing a graphite monochromated using MoKα as a radiation source. Absorption corrections were applied based on the multi-scan method by SADABS software [50]. The structures were solved by direct methods or by the 'dual space' methodology [51] and refined by the full-matrix least-squares technique on F^2 in the anisotropic approximation for non-hydrogen atoms by the SHELXL software [52].

Crystallographic details and processing data of both compounds are compiled in Table 1. Hydrogen atoms were placed in geometrically idealized positions and constrained to ride on their parent atoms with C-H distances in the range 0.95–1.00 Å. All hydrogen atoms were also found in the electron density map confirming the hydrogen placement. Hydrogen atoms on nitrogen in compound (II) were refined isotropically because of the presence of N-H…N hydrogen bonds. All non-hydrogen atoms were refined anisotropically by full-matrix least-squares. Molecular graphics were performed with Diamond [53].

2.3. DFT Calculations

Graphics tools based on the Hirshfeld surface and two-dimensional fingerprints plots used for visualizing and quantifying intermolecular interactions were obtained with the Crystal Explorer software [54]. For Compound (I), two calculations were made, one on the cobalt

complex and the other on the set of the two cations of the crystallographic unit. For Compound (II), the calculations were made on all three elements of the cell in order to take into account possible interactions. All the calculations were made with Gaussian 09 software and the B3LYP method. The basis used for all calculations was 6-31+G*, except for cobalt, for which the LanL2DZ pseudopotential was used. The positions of the atoms are those given by single X-ray diffraction studies, except for the hydrogen atoms, whose positions were optimized beforehand with the B3LYP/6-31+G * method. Frontier orbital localizations and MEP surfaces were obtained with the Molekel software.

2.4. IR Measurement

A Nicolet Impact 410 FT-IR spectrophotometer apparatus was employed to study the infrared spectra of both compounds in the 4000–400 cm^{-1} range. The pellets were prepared by mixing the sample with KBr and compressed into a disk.

2.5. Thermal Study

Thermogravimetric and differential thermal analyses were investigated on a Setaram instrument with a 5°. min^{-1} heating rate under argon atmosphere in the temperature range 273–873 K. The mass of the samples was 9 mg for (I) and 11 mg for (II).

2.6. Antibacterial Methods

A suspension of the tested microorganisms was spread on the appropriate solid media plates and incubated overnight at 37 °C. After 1 day, 4–5 loops of pure colonies were transferred to the saline solution in a test tube for each bacterial strain and adjusted to the 0.5 McFarland turbidity standard (~10^8 cells/mL). Sterile cotton dipped into the bacterial suspension and the agar plates were streaked three times, each time turning the plate at a 60° angle and finally rubbing the swab through the edge of the plate. Sterile paper discs (Glass Microfiber filters, Whatman; 6 mm in diameter) were placed onto inoculated plates and impregnated with the diluted solutions in sterile water. Ampicillin (10 μg/disc) was used as positive control for all

strains except *Candida albicans* for which Nystatin (100 µg/disc) was used. Inoculated plates with discs were placed in a 37 °C incubator. After 24 h of incubation, the results were recorded by measuring the zones of growth inhibition surrounding the disc. Clear inhibition zones around the discs indicated the presence of antimicrobial activity. The tests were run in duplicate.

3. Results and Discussion

3.1. X-ray Diffraction Study

Selected bond lengths and angles are gathered in Table 2. compound (I), with the formula $(HPhPip)_2[Co(NCS)_4]$, crystallizes in the triclinic space group $P\bar{1}$ with Z = 2 (Table 1). Its asymmetric unit consists of a $[Co(NCS)_4]^{2-}$ anion and two 1-phenylpiperazinium cations ($HPhPip^+$), as shown in Fig. 1. The Co^{II} cation is coordinated by four NCS^- anions and resides in the middle of a slightly distorted CoN_4 tetrahedron, whereas two 1-phenylpiperazinium cations ($HPhPip^+$) are placed for charge balancing. The Co–N distances vary between 1.952(3) and 1.972(4) Å, and the angles N–Co–N vary between 102.24 (2) and 117.04(2)° (Table 2). These values are comparable to the reported in $(1\text{-}4\ MPPip)_4[Co(NCS)_4]_2{\cdot}H_2O$ [55]. Considering the crystallographic analysis with latter complex [55], both compounds $(HPhPip)_2[Co(NCS)_4]$ (I) and $(1\text{-}4\ MPPip)_4[Co(NCS)_4]_2{\cdot}H_2O$ are crystallized in the same triclinic space group, while the cell parameters and the hydrogen bond conformations are obviously changed. According to complex (I), the cell parameters as follows : a = 11.497 (5), b = 16.155 (7), c = 19.3921 (10) Å, whereas for $(1\text{-}4\ MPPip)_4[Co(NCS)_4]_2{\cdot}H_2O$ they are: a = 10.5582(11), b = 11.6606(13), c = 12.9724(14)Å. It is worthwhile to note that the methoxy group affects the intermolecular packing. Due to this incorporation, $(1\text{-}4\ MPPip)_4[Co(NCS)_4]_2{\cdot}H_2O$ has more hydrogen bonding making the packing more stable than compound I. In the case of $(1\text{-}4\ MPPip)_4[Co(NCS)_4]_2{\cdot}H_2O$, four $[Co(NCS)_4]^{2-}$ anions, four $(C_{11}H_{17}N_2O)^+$ cations and H_2O interconnected together via N–H…S, O–H…N, O–H…O and

N–H…O hydrogen bonds to generate a three-dimensional assembly. However, in the compound (I) the concerted N–H…S, C–H…S and C−H···π interactions are the main responsible force in the construction of 3D crystalline architecture in solid state.

In the crystallographic bc plane, the $[Co(NCS)_4]^{2-}$ anions are assembled in pairs along the *c*-axis direction (Figure S1), which create anionic layers parallel to the *(a,c)* plane (Fig. 2). The intermetallic distance Co…Co is 6.187(2) Å. As shown in Fig. S2, the N–H atoms of 1-phenylpiperazinium cations form N–H…S hydrogen bonds with the S atoms of adjacent $[Co(NCS)_4]^{2-}$ anions with an average hydrogen bond length N–H…S of 3.328 Å (Table 3). The examination of the atomic arrangement of (I) projected along the crystallographic *a*-axis (Fig. 3) reveals that the organic cations link the $[Co(NCS)_4]^{2-}$ anions via C–H…S interactions (Table 3) to produce a three-dimensional network. Although these interactions are weak compared to the metal–nitrogen coordination bonds, it could be suggested that they are important for the molecular cohesion.

The Co-N-C angles, such as Co1-N5-C21 = 176.0(4), Co1-N6-C22 = 160.0(3), Co1-N7-C23 = 172.5(3), and Co1-N8-C24 = 161.5(3), whose values are far from the expected 180° can be explained by the engagement of S1, S2, S3, and S4 (bonded to C21, C22, C23, and C24, respectively) in H-bonding (Table 3). Compared to other structures having the same $[Co(NCS)_4]^{2-}$ complex, we have found that the Co-N-C angles vary between 129.502° [56] and 180° [57]. In addition, analysis of the crystal packing of (I) shows the presence of C–H···π interactions (Fig. S3) that contribute to the robustness of the solid state of the title compound.

Compound (II), with formula HPhPip(NCS).PhPip, crystallizes in the noncentrosymmetric orthorhombic space group $Pna2_1$ with Z = 2 (Table 1). The correctness of the absolute structure was confirmed by the Flack parameter value of 0.00(8). Its asymmetric unit is composed of one 1-phenylpiperazine molecule, one 1-phenylpiperazinium cation, and one thiocyanate anion, as shown in Fig. 4. The cation forms N–H…N hydrogen bonds and C–

H…S interactions with the neutral molecule and with the anion, respectively (Fig. 5, Table 3), constructing zigzag layers parallel to the ab plane (Fig. 6). The thiocyanate anions are assembled in rows that form anionic layers parallel to the ac plane, as shown in Figure S4. The NCS^{-} anion is linear with an N5–C21–S1 bond angle of 179.3 (2)°. All bond lengths and angles in the 1-phenylpiperazinium cation are within the normal ranges [58]. In the crystal, the $HPhPip^{+}$ and PhPip are linked by strong N–H…N hydrogen bonds (Table 3) in a tail-to-tail manner, leading to parallel chains extending along the *b*-axis direction (Figure S5). This is in agreement with the recently published structure of $(4NH_2PyH)(NCS)\cdot 4NH_2Py$ [59], where N–H…N interactions link the organic entities in the same manner. Fig. S6 shows the C–H···π interactions between the organic cation and the neutral organic molecule with H…plane distances of 3.01(2) and 3.22(2) Å.

The geometric parameters of the organic part in compounds (I) and (II) are reported in Cif file (I) and Table 2, respectively. For salt (II), an examination of these data shows that the bond lengths and angles at the protonated N4 atom were increased (C18-N4 = 1.489(3), C19-N4 = 1.499(2), C18-N4-C19 = 111.54(16) compared with those in neutral 1-Phpip ((C8-N2 = 1.473(3), C9-N2 = 1.470(3), C8-N2-C9 = 109.08(16)) due to the hydrogen-bonding interaction, but these parameters are quite similar to those in compound (II) at the protonated N2 and N4 atoms (C8-N2 = 1.498(5), C9-N2 = 1.486(5), C8-N2-C9 = 109.0(3), C18-N4 = 1.492(5), C19-N4 = 1.486(5), C18-N4-C19 = 110.6(3)).

3.2. Hirshfeld Surface

The Hirshfeld surface is a valuable visualization tool that represents a major advance in enabling supramolecular chemists and crystal engineers to gain insight into packing behaviour. Hirshfeld surface analysis offer a considerable promise method for exploring and identifying features of intermolecular interactions in compounds, as it provides visual images of contacts in a crystalline structure. The Hirshfeld surface reflects the interplay between different atoms

and intermolecular contacts in a crystal. The 3D Hirshfeld surface mapped with d_{norm} and full fingerprint plots of the two compounds $(HPhPip)_2[Co(NCS)_4]$ (I) and (HPhPip)(NCS)·PhPip (II) were made using Crystal Explorer software. The deep red spots visible on the d_{norm} surfaces are indicative of hydrogen-bonding contacts. We conducted the Hirshfeld surface [60] and two-dimensional fingerprint plots [61] in order to determine what types of noncovalent forces contribute to the crystal packing. The visualization of the Hirshfeld three-dimensional d_{norm} surfaces, mapped around each molecule present in the asymmetric units of (I) and (II), are shown in Fig. 7a–c and Fig. 8 a–c, respectively. The enrichment ratios [62–64] between the different chemical species X...X and X…Y highlight which interactions are over-represented in the crystal packing. This ratio is an indicator derived from the Hirshfeld surface analysis. It is defined as a ratio between the proportion of actual contacts in the crystal and the theoretical proportion of random contacts. For (I) and (II), the chemical nature of contacts and their enrichment around each entity in the crystal structures are given in Tables 4 and 5. 2D fingerprint plots are derived from the Hirshfeld surface by plotting the fraction of points on the surface as a function of the pair (d_i, d_e). The percentage contributions from different interatomic contacts to their respective Hirshfeld surfaces are quantitatively summarized in Fig. 9 and 10, respectively. As it can be inferred from crystal structure analyses of the two compounds, they share NCS^- anions as building blocks either connected to the complex of interest or acting as the charge balancing elements of crystal structure. The H...H contacts are the most frequent interactions around both phenylpiperazinium 35.3% and 48.1% (Table 4a,b) due to the abundance of hydrogen on the molecular surface and also explain the interactions between organic molecules in compound (I), but they are slightly under-represented with enrichment ratios of 0.79 and 0.93, respectively, in the two phenylpiperazinium cations (Table 4a,b). Both organic molecules in compound (I) contain 66.5% and 71.75% H and 17.7% and 15.05% C, respectively, on the molecular surfaces. Thus, the H…C contacts represent as much as 33% and

26.1%, respectively, of the interaction surface, and they are over-represented with enrichment ratios >1, confirming the existence of C–H···π interactions in the crystal assembly.

The H…S contacts are the third major interaction in compound (I) around both organic molecules with contributions equal to 12.2% and 17.6%, respectively, due to the sulfur environment imposed by the tetrahedral geometry of tetra(isothiocyanate)cobalt. This contact, with enrichment ratios of $E_{S...H}$ = 1.49 and 1.12 respectively, indicates that cobalt-coordinated sulfur atoms interact with H-atoms of the nitrogen groups. It is responsible for the formation of ring motifs, as shown in Fig. S2, which are connected by one C–H...S and four N–H...S hydrogen bonds in the crystal packing of (I) (Table 3I).

Globally, the N...H interactions are the third most major contacts for the first molecule (C1–C10) that cover 17% of the total Hirshfeld surface and are represented in Figure 8c with red spots confirming the existence of C–H…N interactions in the crystal assembly, which plays a crucial role in building a three-dimensional network. However, this interaction appears with a contribution equal to 3.6% for the second molecule C11–C20. On the other hand, C…C, N...N, C...N, and C...S contacts are impoverished for the first molecule contacts in compound (I) with enrichment ratios of 0.15, 0.43, and 0.38 and 0.04, respectively (Table 4a), the self-contacts S...S and Co...Co are totally absent around both molecules in compound (I) due to electrostatic repulsion (Table 4a,b).

For the anion, it is worthwhile to indicate the abundance of hydrogen with the highest proportion S_H = 41.85% and S_s = 29.05% in the molecular surface. The likelihood to form H…S contacts in the coordination cobalt (II) complex mediated by thiocyanate is highest ($E_{H...S}$ = 1.77), indicating that hydrogen is a preferred partner in contacts made by organic S atoms, as the two atom types are weakly charged and are attractive from an electrostatic point of view. Similarly, the S…Co contacts are over-represented with enrichment ratio equal to 2.98 and contribute to the interactions between inorganic anions.

It is found that the C…H, S...H and N...H interactions are all favored as H atoms are preferred partner of the C, S and N atoms. These interactions correspond to hydrogen bonds formed between the inorganic anion and the C-H/N-H groups of the organic moieties. (Table 4c).

The absence of significant π…π stacking for compound (I) is reflected in $E_{C...C}$ values lower than 0.2 around each entity in the asymmetric unit. Significantly, the C…C contacts are in most cases very disfavored, as they possess a repulsive character. Other enrichment ratios of C...S, C...N, and H...Co interactions are much less to the unity (Table 4c).

In compound (II)**,** the nature of intermolecular interactions has been analyzed around each moiety present in the asymmetric unit in the title compound (II) through Hirshfeld surfaces (Fig. 8). Analysis of the Hirshfeld surface of the organic molecules in the crystal structure mapped with d_{norm} function shows several red areas indicating close contacts between the organic molecules and the thiocyanate anions (Fig. 8). The slight red areas correspond to hydrogen bonds formed between protonated nitrogen atoms of the organic moieties and the sulfur atoms of the thiocyanate anions.

For the second compound, only H...H, C...H, H...S, and H...N are present around both organic entities. H…H interactions represent the strongest contribution with 62.4% and 60.4%, respectively, of the total Hirshfeld surface areas (Fig. 9A,B) due to the presence of plenty of hydrogen in this set of molecules. The $E_{H...H}$ = 0.94 and 0.93, respectively, lower than unity, signifies that this interaction is under-represented and slightly favored statistically. Similarly, the C…H/H…C contacts hold the second major contributions around the three entities present in the asymmetric unit corresponding to 27.7% and 22.1% and 19.6% of each total Hirshfeld surface on this compound (Fig. 10A,B, Table 5a–c). The reason behind such a high percentage is the formation of C–H….π interactions. It can be pointed out that the C–H….π interactions influence the π…π stacking, generating a large distance between the centroid of two

neighboring benzene rings, equal to 4.7 Å (Fig. S6). H…C contacts are generally favored with an enrichment ratio $E_{H...C}$ value of 1.23 and 1.24 for both organic molecules and also around the thiocyanate anions with an enrichment ratio equal to 2.

From this analysis, it can be suggested that the C…H/H…C contacts are a driving force in the molecular arrangement. The breakdown of the fingerprint plot (Fig. 10) shows that the H…S/S…H contacts, which correspond to C–H…S hydrogen bonds (Table 3II), accounting for a high contribution around the anions of 47.2% of the entire Hirshfeld surface (Figure 10C, Table 5c), turn out to be moderately favored and enriched in the crystal packing with an enrichment ratio equal to 1.99. The remaining contribution with 33.1% to the Hirshfeld surfaces is from N…H/H…N contacts, which are responsible for the appearance of deep red spots in the d_{norm} map (Fig. 8C). They are identified by N–H…N hydrogen bond in the crystal lattice. This result indicates that N…H contacts have an increased propensity to form in the crystal packing ($E_{N...H}$ = 1.99).

The crystal packing of both compounds is stabilized through diverse hydrogen bonding interactions. The contributions are from S…H/H…S, N…H/H…N, and C…H/H…C contacts and are significantly higher than unity, showing high propensity to form C–H…S and C–H…N hydrogen bonds, as well as C–H⋯π interactions.

3.3. Quantum Mechanical Study

The frontier molecular orbitals play a major role to assign the electronic properties of the materials. The HOMO and LUMO molecular orbitals in compound (I) were determined for the cobalt complex $Co(SCN)_4$ and the system of the two organic cations, separately (Fig. 11). For the inorganic part, the highest occupied molecular orbital (HOMO) is mainly located on one of the four ligands SCN, while the LUMO is more centered on the cobalt atom. The HOMO–LUMO energy gap is 3.10 eV. The energy distribution of the different orbitals of the $Co(NCS)_4$ entity is displayed in Fig. 12a. For the organic ligand, the HOMO is mainly found

on the aromatic ring and its attached nitrogen atom of one of the two cations, while the LUMO is located on the NH_2 group of the same cation. The energy difference is 3.62 eV. The energy distribution of the different orbitals of the organic entity is represented in Figure 12b. These two large values of energy gap indicate that compound (I) is a hard system with low chemical reactivity.

The HOMO and LUMO orbitals were also determined for compound (II) (Fig. 13a). Orbital contribution investigation indicates that the HOMO is mostly located on the thiocyanate ion, while the LUMO is centered on the NH group of the neutral organic molecule. The HOMO–LUMO energy difference is 3.48 eV, which reflects a greater stability. The energy distribution is depicted in Fig. 13b**.**

3.4. Molecular Electrostatic Potential Analysis

The electrostatic potential is a very treasured property for examining and interpreting molecular reactive behavior. It is an indicator of the sites or regions of a molecule for electrophilic or nucleophilic attacks. According to MEP analysis, the reactive sites are located by different color codes. The red in the MEP graphic signals a negative region showing electrophilic reactivity. However, the blue designates an electron-deficient site, showing nucleophilic reactivity.

The Molecular Electrostatic Potential (MEP) surface for compound (I) is shown in Fig. 14. The maps were obtained at the B3LYP/6–31+G*-LANL2DZ level of theory. For the inorganic part, the positive potential site is around the cobalt atom, while the most negative regions are mainly over carbon and sulfur atoms (Fig. 14a). For the organic cations, the positive zones are on the hydrogen atoms bonded to nitrogen, while the negative zones are located on the aromatic ring (Fig. 14b).

The MEP surfaces of compound (II) were calculated on both the complete system and the isolated molecules (Fig. 15). This clearly shows that the negative areas are located on the thiocyanate ion and the aromatic rings, while the positive zone is located on the hydrogen bonded to nitrogen, in accordance with the Mulliken charges (Tables 5 and 7).

3.5. Mulliken Population Analysis

For Compound (I), the atomic charge distribution shows that, for the $[Co(NCS)_4]^{2-}$ anion, the cobalt ions have positive charge, the most negative atoms being the sulfur and the carbons (Table 5), in agreement with the previous MEP results (Fig. 14a).

The atoms of the organic molecule are numbered as follows:

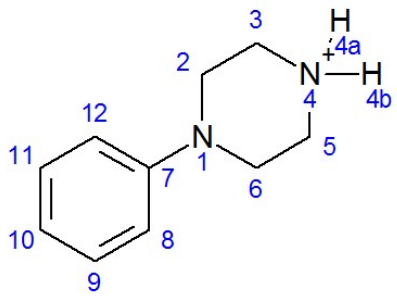

For the piperazine rings of the organic entities, the nitrogen atoms are positively charged, while carbon atoms C2, C3, C5, and C6 have negative charges. For the aromatic rings, the C7 atom has negative charge of -0.559 for Cation 1 and positive charge of 0.003 for cation 2. The C9, C10, and C11 carbon atoms have a negative charge, while the C8 and C12 ones are positively charged. All hydrogen atoms carry positive charge in the range 0.135–0.515 (Table 6).

The Mulliken charges of Compound (II) are given with the same numbering of the atoms as for compound (I). For the piperazine ring of the organic entities, the two nitrogen atoms are positively charged, while carbon atoms C2, C3, C5, and C6 have negative charges. For aromatic rings, the C7 atom has positive charge of 0.036 for the cation and negative charge of -0.042 for the neutral molecule. Contrarily, the C8 atom has negative charge of -0.179 for the cation and positive charge of 0.142 for the neutral molecule. C9, C10, and C11 have negative charges,

while C12 is positively charged. All hydrogen atoms carry positive charge in the range 0.158–0.583 (Table 7). For the thiocyanate anion, the S, C, and N atoms have negative charges (Table 7).

3.6. FT-IR Spectrophotometry

The IR spectra of compounds (I) and (II) are presented in Figs 16a and 17a respectively. In infrared spectroscopy, the presence of the thiocyanate is revealed by an intense peak around 2100 cm^{-1}, which corresponds to the ν(CN) stretching of the thiocyanate moiety [65,66]. According to the literature [67–72], the stretching CN frequencies are observed at 2077 and 2048 cm^{-1} for (I) and (II), respectively. For (I), the strong band at 2077 cm^{-1} is generally attributed to a terminal ambidentate NCS^- ligand bound through the nitrogen atom [73–75]. For (II), the frequency shifting to 2048 cm^{-1} suggests the presence of NCS groups involved in a system of hydrogen bonds in the crystal. The frequency of this mode is shifted toward lower values due to the establishment of hydrogen bonds. The strong band corresponding to the C=S stretching mode appears at 763 and 769 cm^{-1} for (I) and (II), respectively. The absorption bands observed at 470 cm^{-1} in the IR spectra of both compounds are assigned to the δ (NCS) bending mode. The spectra of (I) and (II) also show the characteristic vibrations for 1-phenylpiperazinium cation. The spectra of the two compounds show strong intensity bands in the range of 3147–3111 cm^{-1} corresponding to the stretching vibrations ν (N–H) and ν(C–H). The bands in the 1640–1300 cm^{-1} regions correspond to the N–H bending modes of NH_2^+ and NH^+ and the aromatic ring. The bending vibrations of N–H appear at 1637 and 1634 cm^{-1} for (I) and (II), respectively. The peaks located at 1450 and 1392 cm^{-1} for (I) and 1450 and 1376 cm^{-1} for (II) are assigned to the asymmetric and symmetric stretching vibration modes of C–N, respectively. The absorption bands in the region of 1300–1040 cm^{-1} are ascribed to the stretching vibrations of (C–C) and (C–H) and to the δ(C–H) in plane deformation. The weak band around 916 cm^{-1} corresponds to the ring deformation. The bands between 900 and 700

cm^{-1} are assigned to the out-of-plane bending modes δ(C–N), δ(C–H), and δ(C–C). Finally, bands between 700 and 500 cm^{-1} are assigned to the CH_2 rocking [76].

The IR spectra of compounds (I) and (II) were calculated by use of the B3LYP/6-31+G* method. The positions of the protons were first optimized as the data of the X-ray study led to numerous imaginary frequencies, the X–H distances being too short. The resulting IR spectra between 4000 and 400 cm^{-1}, shown in Figs 16b and 17b, are very similar to the experimental ones. A close agreement between experimental and calculated values (R = 0.9993 for (I) and R = 0.9958 for (II)) of wavenumbers is mostly achieved, as shown in Figure 18. Thus, the precision is well-sufficient to assign the experimental frequencies and to verify the attributions proposed above.

3.7. Thermal Analysis

The thermal behavior of the two compounds was carried out using TG-DTA with heating from 273 to 873 K at 5 K. min^{-1} under argon atmosphere. The TG-DTG curves of both complexes $(HPhPip)_2[Co(NCS)_4]$ (I) and (HPhPip)(NCS)·PhPip (II) are shown in Fig. 19.

For Compound (I), the first peak in the DTA curve occurs at 393 K without mass loss observed on the ATG curve, could probably be attributed to a phase transition (Fig. 19a). The DTA curve of (I) undergoes decomposition in two steps within the temperature range 533–743 K. The first decomposition step located at 542 K with a weight loss of 23.24% was accounted for the removal of two 1-phenylpiperazine molecules. The second step occurs at higher temperatures and corresponds to the loss of any NCS^- ligands. Figure 19b shows the results of TG-DTA measurements of (II). The thermal decomposition involves three major processes. The two consecutive steps observed in the DTA curve at 428 and 490 K correspond to the loss of the thiocyanate ligands. These peaks have a weight loss of 14.33% detected in the TG curve (calculated weight of 15.14%). The last two exothermic peaks correspond to the pyrolysis as well as the decomposition of the organic part. Over this wide temperature range from 683 to

900 K, the sample gradually loses additional 85% weight, which may be interpreted in terms of liberating two organic molecules (calculated value Δm = 84. 85%).

It is clear that the stability of the compounds decreases due to the presence of transition metal. Obviously, the thermal stability was affected by the electronegativity of the central metal atom. On the one hand, complex (I) goes through a phase transition at 393 K. On the other hand, compound (II) shows good thermal stability until 425 K.

3.8. Antibacterial Activity

The antibacterial activity is an important tool to evaluate the potential of compounds to inhibit the progression of pathogenic bacteria. Investigation of the antibacterial capacity was carried out for both compounds by using disk diffusion assay against different types of bacteria such as *Escherichia coli, Salmonella typhimurium, Enterococcus faecium,* and *Candida albicans*. Results and graphical representation of the two tested compounds are given in Table 8. Nevertheless, bioactivities of two compounds are lower than the commercial control tested. The cobalt compound (I) have a moderate antibacterial effect, while compound (II) exhibits a significantly weaker effect against the growth of bacteria. These differences indicate the influence of the metal transition on the antibacterial activity where the cobalt metal compound (I) is more effective and possesses a moderate biological effect than Compound (II). From these results, it can be deduced that the bactericidal property is greatly bolstered on complexation with the cobalt ion.

Compared to previously reported analogous complexes [76], the antibacterial activity for all tests (*Escherichia coli, Salmonella typhimurium, Enterococcus faecium,* and *Candida albicans*) has comparable values (Table 9), since both complexes have a similar organic part. The antibacterial activity of compound (II) is less important than compound (I). This disparency can be explained in terms of nature of the metal ion, metal ion coordinating site and presence

of coligands. It is interesting to note that both complexes showed increased antifungal activity than other complexes against *Candida albicans*. These compounds were found to be efficient antifungal agents.

4. Conclusions

In the current research, we have described the synthesis and physicochemical characterizations of two new compounds $(HPhPip)_2[Co(NCS)_4]$ (I) and (HPhPip)(NCS)·PhPip (II). The molecular stability of both compounds was expressed by hydrogen bonding and C–H…π interactions, resulting in a three-dimensional network. The intermolecular interactions held out in the crystal assembly were visually interpreted through Hirshfeld surfaces, associated 2D fingerprint plots, and enrichment ratios. FT-IR spectral data of both compounds supported by quantum chemical calculations confirm the structural assignment. The electronic properties of materials were examined by means of the frontier molecular orbital analysis. The HOMO–LUMO energy gaps have appreciable impact on the chemical stability of materials. The molecular electrostatic potential of the two compounds determined the nucleophilic and electrophilic sites. Furthermore, the antibacterial screening assay of the compounds revealed higher activity of the metal complex than compound (II) toward four bacterial strains. Finally, the thermal stability was investigated by TGA–DTA. This study reveals that compound (I) undergoes a phase transition at 393 K, while compound (II) can stay in its solid phase up to 428 K.

Author Contributions: Chaima Gharbi: Synthesis of the compounds, Writing – original draft Baya Toumi: Ressources, Sarra Soudani: Software, Frédéric Lefebvre: Quantum mechanical study, Werner Kaminsky: X-ray data collections and structure resolution, Christian Jelsch: Hirshfeld surface and contacts enrichment study, Chérif Ben Nasr: Writing – review and

editing. Lamia Khedhiri: Writing – review, editing and supervision. All authors have read and agreed to the published version of the manuscript

Funding: This research received no external funding.

Data Availability Statement: Crystallographic data for the structural analysis have been deposited at the Cambridge Crystallographic Data Centre, CCDC No 2072863 for Compound (I) and 2072865 for Compound (II). These data can be obtained free of charge via http://www.ccdc.cam.ac.uk/conts/retrieving.html, or from the CCDC, 12 Union Road, Cambridge, CB2 1EZ, UK: fax: (+44) 01223-336-033; e-mail: deposit@ccdc.cam.ac.

Conflicts of Interest: The authors declare no conflict of interest

References

[1] T. Yousef, G. Abu El-Reash, M. Abu Al-Zahab, M. Safaan, Physicochemical investigations, biological studies of the Cr(III), Mn(II), Fe(III), Co(II), Ni(II), Cu(II), Zn(II), Cd(II), Hg(II) and UO_2(VI) complexes of picolinic acid hydrazide derivative: A combined experimental and computational approach. J. Mol. Struct. 1197 (2019) 564–575. https://doi.org/10.1016/j.molstruc.2019.07.088.

[2] M. A. Zakharov, Y. V. Filatova, M. A. Bykov, N. V. Avramenko, L. A. Aslanov, Synthesis, Crystal Structures, and Thermal Properties of Protic Metal-Containing Ionic Liquids, Diethanolammonium Halometallates: $(HOCH_2CH_2)_2NH_2FeCl_4$ and $((HOCH_2CH_2)_2NH_2)_2CoCl_4$. Russ. J. Coord. Chem. 46 (2020) 268–275. https://doi.org/10.1134/s1070328420040077.

[3] D. Dittrich, H. Tewes, C. Wölper, D. Bläser, S. Schulz, J. Roll, Preparation, catalytical activity and crystal structure of a heptanuclear zinc acetate cluster. Transit. Met. Chem. 42 (2017) 237–241. https://doi.org/10.1007/s11243-017-0127-y.

[4] P. A. Demakov, S. A. Sapchenko, D. G. Samsonenko, D. N. Dybtsev, V. P. Fedin, Coordination polymers based on zinc(II) and manganese(II) with 1,4-cyclohexanedicarboxylic acid. Russ. Chem. Bull. 67 (2018) 490–496. https://doi.org/10.1007/s11172-018-2098-3.

[5] S. Li, J.-X. Chen, Q.-X. Xiang, L.-Q. Zhang, C.-H. Zhou, J.-Q. Xie, L. Yu, F.- Z. Li, The synthesis and activities of novel mononuclear or dinuclear cyclen complexes bearing azole pendants as antibacterial and antifungal agents. Eur. J. Med. Chem. 84 (2014) 677–686. https://doi.org/10.1016/j.ejmech.2014.07.075

[6] U. O. Ozdemir, N. Ozbek, Z. K. Genc, F. Ilbiz, A. B. Gündüzalp, New bioactive silver(I) complexes: Synthesis, characterization, anticancer, antibacterial and

anticarbonic anhydrase II activities. J. Mol. Struct. 1138 (2017) 55–63. https://doi.org/10.1016/j.molstruc.2017.02.101.

[7] S. Chandra, Vandana, S. Kumar, Synthesis, spectroscopic, anticancer, antibacterial and antifungal studies of Ni(II) and Cu(II) complexes with hydrazine carboxamide, 2-[3-methyl-2-thienyl methylene]. Spectrochim. Acta Part A Mol. Biomol. Spectrosc. 135 (2015) 356–363. https://doi.org/10.1016/j.saa.2014.06.143.

[8] H.-Q. Chang, L. Jia, J. Xu, Z.-Q. Xu, R.-H. Chen, W.-N. Wu, H.-Y. Bie, T.- F. Zhu, T.-L. Ma, Y. Wang, Syntheses, characterizations, antitumor activities and cell apoptosis induction of Cu(II), Zn(II) and Cd(II) complexes with hydrazone Schiff base derived from isonicotinohydrazide. Inorg. Chem. Commun. 57 (2015) 8–10. https://doi.org/10.1016/j.inoche.2015.04.010.

[9] L. Jia, J. Xu, X. Zhao, S. Shen, T. Zhou, Z. Xu, T. Zhu, R. Chen, T. Ma, J. Xie, Synthesis, characterization, and antitumor activity of three ternary dinuclear copper (II) complexes with a reduced Schiff base ligand and diimine coligands in vitro and in vivo. J. Inorg. Biochem. 159 (2016) 107–119. https://doi.org/10.1016/j.jinorgbio.2016.02.033.

[10] X.-Z. Zou, J.-A. Zhang, L.-J. Zhang, Y.-J. Liu, N. Li, Y. Li, S.-C. Wei, M. Pan, Crystal structures and biological activities of a symmetrical quinoline thioether ligand and its transition metal complexes. Inorg. Chem. Commun. 54 (2015) 21–24. https://doi.org/10.1016/j.inoche.2015.01.029.

[11] M. S. Muneera, J. Joseph, Design, synthesis, structural elucidation, pharmacological evaluation of metal complexes with pyrazoline derivatives. J. Photochem. Photobiol. B: Biol. 163 (2016) 57–68. https://doi.org/10.1016/j.jphotobiol.2016.08.010.

[12] D. P. Singh, D. S. Raghuvanshi, K. N. Singh, V. P. Singh, Synthesis, characterization and catalytic application of some novel binuclear transition metal complexes of bis-(2-

acetylthiophene) oxaloyldihydrazone for C-N bond formation. J. Mol. Catal. A Chem. 379 (2013) 21–29.

[13] J. Mondal, A. Dutta, P. K. Pal, R. Saha, P. Maji, G. K. Patra, Synthesis, structure, photo-physical properties and catalytic activities of Zn(II), Cd(II) and Hg(II) complexes of an azinopyridyl ligand. Inorg. Chim. Acta 448 (2016) 70–77. https://doi.org/10.1016/j.ica.2016.04.026.

[14] A. Laachir, F. Rhoufal, S. Guesmi, E. M. Ketatni, L. Jouffret, E. K. Hlil, N. Sergent, S. Obbade, F. Bentiss, Cobalt(II) coordination complex with 2,5-bis(pyridine-2-yl)-1,3,4-thiadiazole and thiocyanate as co-ligand: Synthesis, crystal structure, Hirshfeld surface analysis, spectroscopic, thermal and magnetic properties. J. Mol. Struct. 1208 (2020) 127892. https://doi.org/10.1016/j.molstruc.2020.127892.

[15] A. K. Renfrew, E. S. O'Neill, T. W. Hambley, E. J. New, Harnessing the properties of cobalt coordination complexes for biological application. Coord. Chem. Rev. 375 (2017) 221–233.

[16] S. Okamoto, L. D. Eltis, The biological occurrence and trafficking of cobalt. Metallomics 3 (2011) 963–970. https://doi.org/10.1039/c1mt00056j.

[17] F. E. Meva, T. J. Prior, D. J. Evans, S. Shah, O. Cespedes, Iron(III), cobalt(II) and zinc(II) coordination compounds with a car-boximidamide ligand: Synthesis, structures and properties. Inorg. Chem. Commun. 121 (2020) 108196.

[18] A. Adach, M. Daszkiewicz, M. Tyszka-Czochara, Comparative X-ray, vibrational, theoretical and biological studies of new in situ formed $[CoLSX]_2[CdX_4]$ halogenocadmate(II) complexes containing an N–scorpionate ligand Polyhedron 175 (2020) 114229. https://doi.org/10.1016/j.poly.2019.114229.

[19] Q.-Q. Yan, B. Li, G.-P. Yong, Co(II) and Mn(II) coordination polymers: Ligand functional and positional isomeric effects, structural diversities, luminescence sensing

and magnetic properties. Polyhedron 194 (2020) 114918. https://doi.org/10.1016/j.poly.2020.114918.

[20] H. Zhang, X. M. Wang, K. C. Zhang, B. K. Teo, Molecular and crystal engineering of a new class of inorganic cadmi-um-thiocyanate polymers with host–guest complexes as organic spacers, controllers, and templates. Coord. Chem. Rev. 183 (1999) 157–195.

[21] S. S. Kaye, J. R. Long, Hydrogen Storage in the Dehydrated Prussian Blue Analogues $M_3[Co(CN)_6]_2$ (M = Mn, Fe, Co, Ni, Cu, Zn). J. Am. Chem. Soc. 127 (2005) 6506–6507. https://doi.org/10.1021/ja051168t.

[22] A. Galet, M. C. Muñoz, A. B. Gaspar, J. A. Real, Architectural Isomerism in the Three-Dimensional Polymeric Spin Crossover System $\{Fe(pmd)_2[Ag(CN)_2]_2\}$: Synthesis, Structure, Magnetic Properties, and Calorimetric Studies. Inorg. Chem. 44 (2005) 8749–8755.

[23] S. J. Munshi, M. H. Sadhu, S. Kundu, C. Savani, S. B. Kumar, Synthesis, characterization and structures of binuclear copper(II) and polynuclear cobalt(II), nickel(II) and cadmium(II) complexes involving N4-donor pyrazolyl based ligand and dicyana-mide as bridging ligand. J. Mol. Struct. 1209 (2020) 127984.

[24] Z. Zhang, J. Xu, S. Yan, Y. Chen, Y. Wang, Z. Chen, C. L. Ni, Two Organic Cation Salts Containing Tet-ra(isothiocyanate)cobaltate(II): Synthesis, Crystal Structures, Spectroscopic, Optical and Magnetic Properties. Crystals 7 (2017) 92–105.

[25] A. Hannachi, A. Valkonen, M. Rzaigui, W. Smirani, Thiocyanate precursor impact on the formation of cobalt complexes: Synthesis and characterization. Polyhedron 161 (2019) 222–230. https://doi.org/10.1016/j.poly.2018.12.039.

[26] R. D. Pike, T. M. Dziura, J. C. Debutts, C. A. Murray, A. T. Kerr, C. L. Cahill, Copper(I) Cyanide Networks with 1-Phenylpiperazine. J. Chem. Crystallogr. 44. (2014) 42–50. https://doi.org/10.1007/s10870-013-0482-2.

[27] F. Zouari, A. Ben Salah, E. R. Hovestreydt, Phenylpiperazinium Trichloromercurate. Acta Crystallogr. Sect. C Cryst. Struct. Commun. 51 (1995) 1563–1565. https://doi.org/10.1107/s0108270194013454.

[28] Y.Oueslati, S.Kansız, A.Valkonen, T.Sahbani, N. Dege, W. Smirani, Synthesis, crystal structure, DFT calculations, Hirshfeld surface, vibrational and optical properties of a novel hybrid non-centrosymmetric material $(C_{10}H_{15}N_2)_2H_2P_2O_7$. J. Mol. Struct. 1196 (2019), 499–507. https://doi.org/10.1016/j.molstruc.2019.06.110.

[29] M. Mathlouthi, A. C. Dhieb, A. Valkonen, M. Rzaigui, W. Smirani, Crystal Structure, Dielectric Characteristics and Conduction Mechanism of a New Hybrid Material, Tetra(Phenylpiperazinium) Decachlorotriplumbate(II). J. Clust. Sci. 28 (2017) 3159–3174.

[30] Y. Pang, P. Xing, X. Geng, Y. Zhu, F. Liu, L. Wang, Supramolecular assemblies of 2-hydroxy-3-naphthoic acid and N-heterocycles via various strong hydrogen bonds and weak X···π (X = C–H, π) interactions. RSC Adv. 51 (2015) 40912–40923.

[31] M. Essid, H. Marouani, M.Rzaigui, S. S. Al-Deyab, 4-Phenylpiperazin-1-ium dihydrogen phosphate. Acta Crystallogr. Sect. E Struct. Rep. Online 66 (2010) o2244–o2245. https://doi.org/10.1107/S1600536810030813.

[32] H.-Y. Bie, J. Lu, J.-H. Yu, J.-Q. Xu, K. Zhao, X. Zhang, Syntheses of fluorescent thiocyanate supramolecular compounds with unusual two-dimensional structures. J. Solid State Chem. 178 (2005) 1445–1451. https://doi.org/10.1016/j.jssc.2005.01.027.

[33] L. P. Battaglia, A. B. Corradi, G. Marcotrigiano, L. Menabue, G. C. Pellacani, Halocuprates(II) of the N-phenylpiperazinium mono- and dications: Crystal and

molecular structure of N-phenylpiperazinium tetrachloro cuprate(II). Correlation of the electronic spectrum vs. distortion of the $CuCl_4^{2-}$ anions from tetrahedral symmetry. Inorg. Chem. 18 (1979) 148–152. https://doi.org/10.1021/ic50191a031.

[34] A. C. Dhieb, D. Janzen, M. Rzaigui, W. S. Sta, 1-Phenylpiperazine-1,4-diium tetrachloridocobalt(II). Acta Crystallogr. Sect. E Struct. Rep. Online 70 (2014) m139. https://doi.org/10.1107/s1600536814005790.

[35] A. C. Dhieb, A. Valkonen, M. Rzaigui, W. Smirani, Synthesis, crystal structure, physicochemical characterization and dielectric properties of a new hybrid material, 1- Ethylpiperazine-1,4-diium tetrachlorocadmate. J. Mol. Struct. 1102 (2015) 50–56.

[36] H. Marouani, M. Rzaigui, S. S. Al-Deyab, 1-Phenylpiperazine-1,4-diium bis(hydrogen sulfate). Acta Crystallogr. Sect. E Struct. Rep. Online 66 (2010) o2613. https://doi.org/10.1107/S1600536810037001.

[37] R. S. Upadhayaya, N. Sinha, S. Jain, N. Kishore, R. Chandra, S. K. Arora, Optically active antifungal azoles: Synthesis and antifungal activity of (2R,3S)-2-(2,4-difluorophenyl)-3-(5-{2-[4-aryl-piperazin-1-yl]-ethyl}-tetrazol-2-yl/1-yl)-1-[1,2,4]-triazol-1-yl-butan-2-ol. Bioorg. Med. Chem. 12 (2004) 2225–2238.

[38] W. O. Foye, T. L. Lemke, D. A. William, Principles of Medicinal Chemistry, 4th ed.; Williams and Wilkins: London, UK, 1995.

[39] L. L. Gan, Y. H. Lu, C. H. Zhou, Advances in the research of piperazine compounds as enzyme inhibitors Chin. J. Biochem. Pharm. 30 (2009) 127–131.

[40] J. L. Cai, Lu, Y. H. Gan, L. L. Zhang, Y. Y. Zhou, C. H. Recent advance in the research of piperazine-containing compounds as antimicrobial agents. Chin. J. Antibiot 34 (2009) 454–462.

[41] L. L. Gan, J. L. Cai, C. H. Zhou, Advances in the research of piperazine compounds as receptor ligands. Chin. Pharma J. 44 (2009) 1361–1368..

[42] G. M. Badger, The Chemistry of Heterocyclic Compounds; Academic Press: New York, NY, USA; London, UK, 1961; p. 233.

[43] S. Bhati, V. Kumar, S. Singh, J. Singh, Synthesis, biological activities and docking studies of piperazine incorporated 1, 3, 4-oxadiazole derivatives. J. Mol. Struct. 1191 (2019) 197–205. https://doi.org/10.1016/j.molstruc.2019.04.106.

[44] K. Kulig, J. Sapa, D. Maciag, B. Filipek, B. Malawska, Synthesis and Pharmacological Evaluation of New 1-[3-(4-Arylpiperazin-1-yl)-2-hydroxypropyl]-pyrrolidin-2-one Derivatives with Anti-arrhythmic, Hypotensive, and α-Adrenolytic Activity. Arch. Pharm. 340 (2007) 466–475. https://doi.org/10.1002/ardp.200700039.

[45] S. F. Mccullagh, Allergenicity of Piperazine: A Study in Environmental Aetiology. Occup. Environ. Med. 25 (1968) 319–325. https://doi.org/10.1136/oem.25.4.319.

[46] A. Pietrzycka, M. Stepniewski, A. M. Waszkielewicz, H. Marona, Preliminary evaluation of antioxidant activity of some 1-(phenoxyethyl)-piperazine derivatives. Acta Pol. Pharm. Drug Res. 63 (2007) 19–24.

[47] L. L. Brockunier, J. He, L. F. Colwell Jr., B. Habulihaz, H. He, B. Leiting, K. A. Lyons, F. Marsilio, R. A. Patel, Y. Teffera, Substituted piperazines as novel dipeptidyl peptidase IV inhibitors. Bioorg. Med. Chem. Lett. 14 (2004) 4763–4766.

[48] E. Bogatcheva, C. Hanrahan, B. Nikonenko, R. Samala, P. Chen, J. Gearhart, F. Barbosa, L. Einck, C. A. Nacy, M. Protopopova, Identification of New Diamine Scaffolds with Activity againstMycobacterium tuberculosis. J. Med. Chem. 49 (2006) 3045–3048. https://doi.org/10.1021/jm050948+.

[49] R. Kharb, K. Bansal, A. K. Sharma, A Valuable insight into recent advances on antimicrobial activity of piperazine derivatives. Pharma. Chem. 4 (2012) 2470–2488.

[50] G. M. Sheldrick, SADABS, Program for Empirical Absorption Correction of Area Detector Data; University of Göttingen: Göttingen, Germany, 1996.

[51] G. M. Sheldrick, SHELXT—Integrated space-group and crystal-structure determination. Acta Crystallogr. Sect. A Found. Adv. 71 (2015) 3–8. https://doi.org/10.1107/s2053273314026370.

[52] G. M. Sheldrick, A short history of SHELX. Acta Cryst. A 64 (2008) 112–122.

[53] K. Brandenburg, DIAMOND Version 2.0; 1998. Impact GbR. Bonn, Germany

[54] J. J. McKinnon, M. A. Spackman, A. S. Mitchell, Novel tools for visualizing and exploring intermolecular interactions in molecular crystals. Acta Crystallogr. Sect. B Struct. Sci. 60 (2004) 627–668. https://doi.org/10.1107/s0108768104020300.

[55] C. Gharbi,; W. Fujita,; F. Lefebvre,; W. Kaminsky,; C. Jelsch,; C. Ben Nasr,; L. Khedhiri, Synthesis, crystal structure, computational studies and spectroscopic characterization of a hybrid material self-assembly from tetra(isothiocyanate)cobalt(II) anion and 1-(4-methoxyphenyl)piperazinium. J. Mol. Struct. 1230 (2021) 129929.

[56] S. Banerjee, A. Ray, S. Sen, S. Mitra, D. L. Hughes, R. J. Butcher, S. R. Batten, D. R. Turner. Pseudohalide-induced structural variations in hydrazone-based metal complexes: Syntheses, electrochemical studies and structural aspects. Inorg. Chim. Acta 361 (2008) 2692-2700

[57] G. Vlahopoulou, A. Escuer, M. Font-Bardia, T. Calvet. Synthesis and characterization of CoIII3 inverse metallacrowns via use of 6-methyl-2-pyridylaldoxime. Inorg. Chem. Commun. 16 (2012) 78-80

[58] L. Khedhiri, A. Hamdi, S. Soudani, W. Kaminsky, F. Lefebvre, C. Jelsch, M. Wojtaś, C. Ben Nasr, Crystal structure, hirshfeld surface analysis, thermal behavior and spectroscopic investigations of a new organic cyclohexaphosphate, $(C_{10}H_{15}N_2)_4(Li)_2(P_6O_{18})$ $(H_2O)_6$. J. Mol. Struct. 1171 (2018) 429–437. https://doi.org/10.1016/j.molstruc.2018.06.015.

[59] M. Renugadevi, A. Sinthiya, K. Poomani, S. Suresh, Crystal structure and Hirshfeld surface analysis of 4-aminopyridinium thiocyanate–4-aminopyridine (1/1). Acta Crystallogr. Sect. E Crystallogr. Commun. 76 (2020) 1535–1538. https://doi.org/10.1107/s2056989020011445.

[60] J. J. McKinnon, D. Jayatilaka, M. A. Spackman, Towards quantitative analysis of intermolecular interactions with Hirshfeld surfaces. Chem. Commun. 37 (2007), 3814–3816. https://doi.org/10.1039/b704980c.

[61] M. A. Spackman, D. Jayatilaka, Hirshfeld surface analysis. Cryst. Eng. Comm. 11. (2009), 19–32.

[62] A. Di Santo, H. Pérez, G. A. Echeverría, O. E. Piro, R. A. Iglesias, R. E Carbonio,. A. Ben Altabef, D. M. Gil, Exploring weak intermolecular interactions in thiocyanate-bonded Zn(II) and Cd(II) complexes with methylimidazole: Crystal structures, Hirshfeld surface analysis and luminescence properties. RSC Adv. 8 (2018) 23891–23902. https://doi.org/10.1039/c8ra04452j.

[63] M. G. Babashkina, K. Robeyns, Y. Filinchuk, D. A. Safin, Detailed studies of the interaction of 3-chloroaniline with O,O′-diphenylphosphorylisothiocyanate. New J. Chem. 40 (2016) 1230–1236. https://doi.org/10.1039/c5nj02588e.

[64] C. Jelsch, S. Soudani, C. Ben Nasr, Likelihood of atom–atom contacts in crystal structures of halogenated organic compounds. *Chem. Cryst. Eng 2 (*2015) 327–340. https://doi.org/10.1107/s2052252515003255.

[65] L. Shen, Y. Z. Xu, Structure and magnetic properties of a novel two-dimensional thiocyanato-bridged heterometallic polymer $\{Cu(en)_2[Ni(en)(SCN)_3]_2\}_n$. J. Chem. Soc. Dalton Trans. 23 (2001) 3413–3414.

[66] S. Wöhlert, C. Näther, New cobalt and nickel thiocyanato coordination polymers with pyridazine: Synthesis, structure and desolvation/resolvation behavior. Polyhedron 52 (2013) 1073–1080. https://doi.org/10.1016/j.poly.2012.06.071.

[67] H.-Q. Ye, Y.-Y. Li, R.-K. Huang, X.-P. Liu, W.-Q. Chen, J.-R. Zhou, L.-M. Yang, C.-L. Ni, Unusual layer structure in an ion-paired compound containing tetra(isothiocyanate) cobalt(II) dianion and 4-nitrobenzylpyridinium: Crystal structure and magnetic properties. J. Struct. Chem. 55 (2014) 691–696. https://doi.org/10.1134/s0022476614040143.

[68] H.-T. Cai, Q.-T. Liu, H.-Q. Ye, L.-J. Su, X.-X. Zheng, J.-N. Li, S.-H. Ou, J.-R. Zhou, L.-M. Yang, C.-L. Ni, Syntheses, crystal structures, luminescent and magnetic properties of two molecular solids containing naphthylmethylene triphenylphosphinium cations and tetra(isothiocyanate)cobalt(II) dianion. Spectrochim. Acta Part A Mol. Biomol. Spectrosc. 142 (2015) 239–245. https://doi.org/10.1016/j.saa.2015.01.098.

[69] G. M. Ionita, G. Ilie, C. Angel, F. Dan, D. K. Smith, V. Chechik, Sorption of Metal Ions by Poly(ethylene glycol)/β-CD Hydrogels Leads to Gel-Embedded Metal Nanoparticles. Langmuir 29 (2013) 9173–9178.

[70] S. J. Osborne, S. Wellens, C. Ward, S. Felton, R. M. Bowman, K. Binnemans, M. Swadźba-Kwaśny, H. Q. N. Gunaratne, P. Nockemann, Thermochromism and switchable paramagnetism of cobalt(II) in thiocyanate ionic liquids. Dalton Trans. 44 (2015) 11286–11289. https://doi.org/10.1039/C5DT01829C.

[71] A. A. Bagabas, M. Alsawalha, M. Sohail, S. Alhoshan, R. Arasheed, Synthesis, crystal structure, and characterization of cyclohexylammonium tetraisothiocyanatocobaltate (II): A single-source precursor for cobalt sulfide and oxide nanostructures. Heliyon 5 (2019) e01139.

[72] S. S. Massoud, L. Le Quan, K. Gatterer, J. H. Albering, R. C. Fischer, F. A. Mautner, Structural characterization of five-coordinate copper (II), nickel (II), and cobalt (II) thiocyanato complexes derived from bis (2-(3,5-dimethyl-1-pyrazolyl) ethyl) amine. *Polyhedron 31 (*2012) 601–606.

[73] R. Uhrecky, I. Ondrejkovicová, D. Lacková, Z. Fáberová, J. Mrozinski, B. Kalinska, Z. Padelková, M. Koman, New thiocyanato iron (II) complex with 3,5-bis(3-pyridyl)-1,2,4-thiadiazole: Synthesis, structure, magnetic and spectral properties Inorg. Chim. Acta, 414 (2014) 33–38.

[74] P. Mukherjee, C. Biswas, M. G. Drew, A. Ghosh, Structural variations in Ni(II) complexes of salen type di-Schiff base ligands. Polyhedron 26 (2007) 3121–3128. https://doi.org/10.1016/j.poly.2007.02.006.

[75] A. Hazari, L. K. Das, A. Bauzá, A. Frontera, A. Ghosh, The influence of H-bonding on the 'ambidentate' coordination behaviour of the thiocyanate ion to Cd(II): A combined experimental and theoretical study. Dalton Trans. 43 (2014) 8007–8015.

[76] A. Hannachi, A. Valkonen, C. J. G. García, M. Rzaigui, W. Smirani, Synthesis of isomorphous cobalt and nickel thiocyanate coordination compounds: Effect of metals on compound properties. Polyhedron 173 (2019) 114122. https://doi.org/10.1016/j.poly.2019.114122.

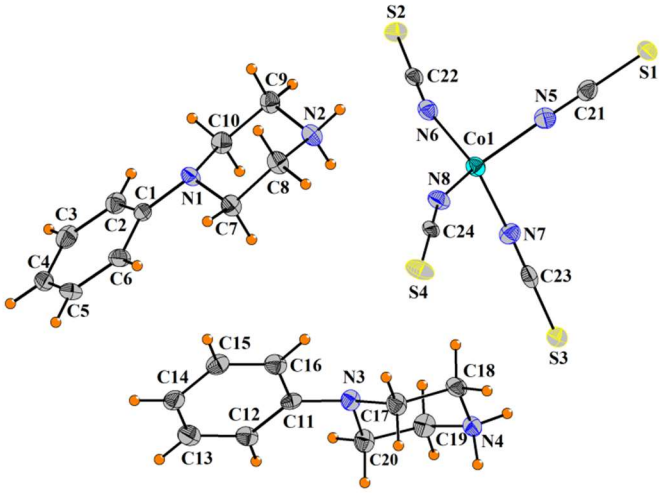

Fig. 1: ORTEP of **(I)** with displacement ellipsoids drawn at the 40% probability level.

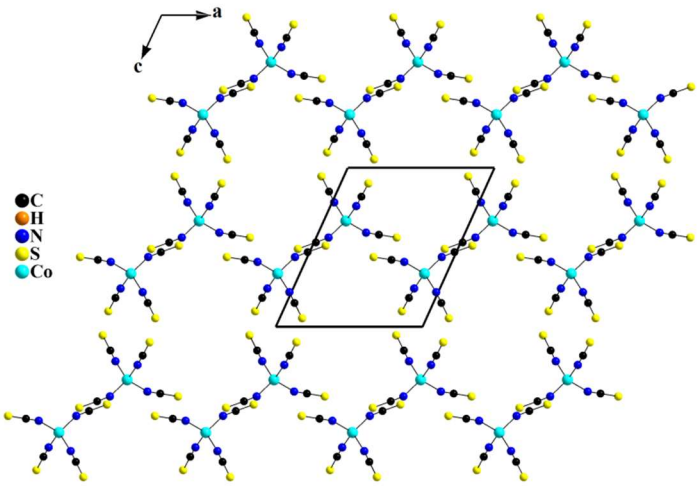

Fig. 2: $Co(SCN)_4$ moieties forming a layer parallel to the (a,c) plane in (I).

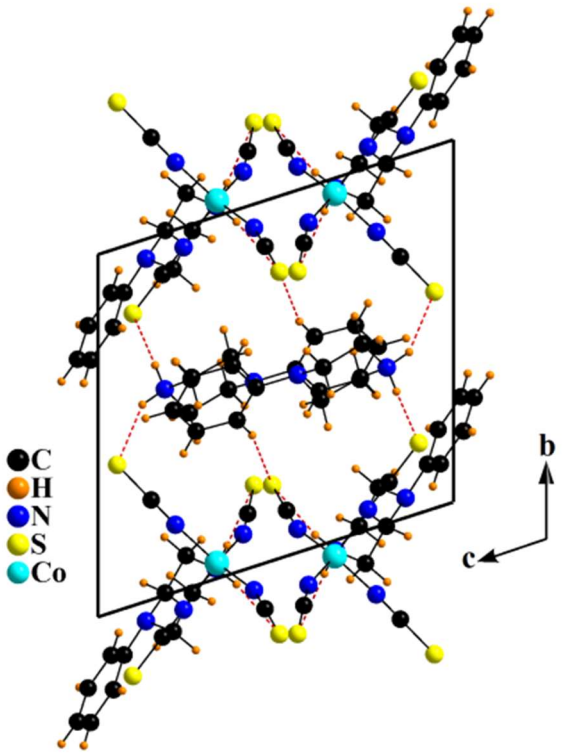

Fig. 3: Projection along the *a*-axis of the structure of (I).Dotted lines indicate hydrogen bonds.

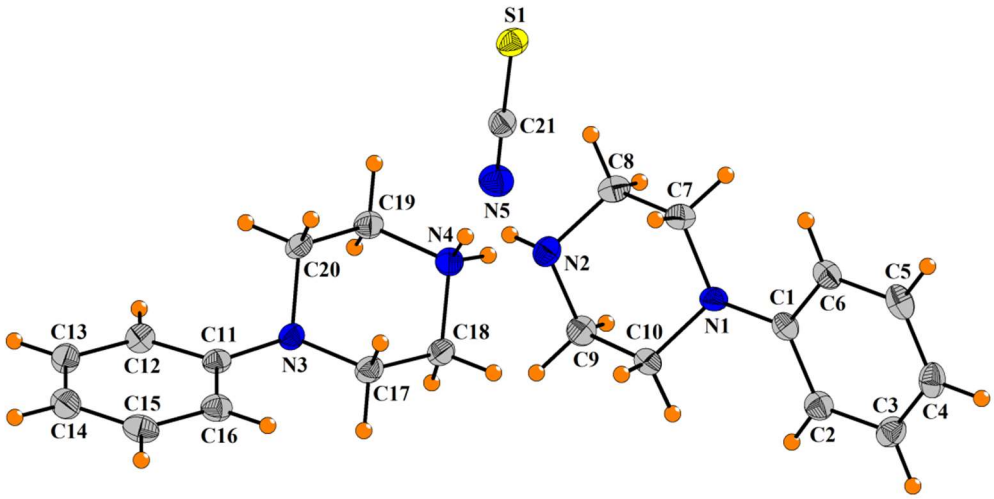

Fig. 4: ORTEP of (II) with displacement ellipsoids drawn at the 40% probability level.

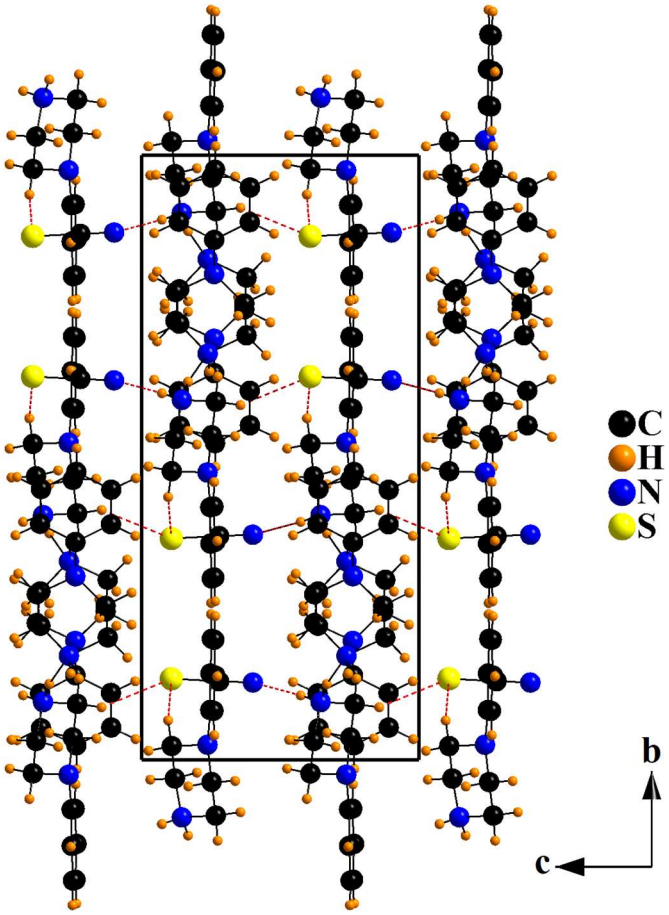

Fig. 5: Projection of the structure of (II) along the *a*-axis.

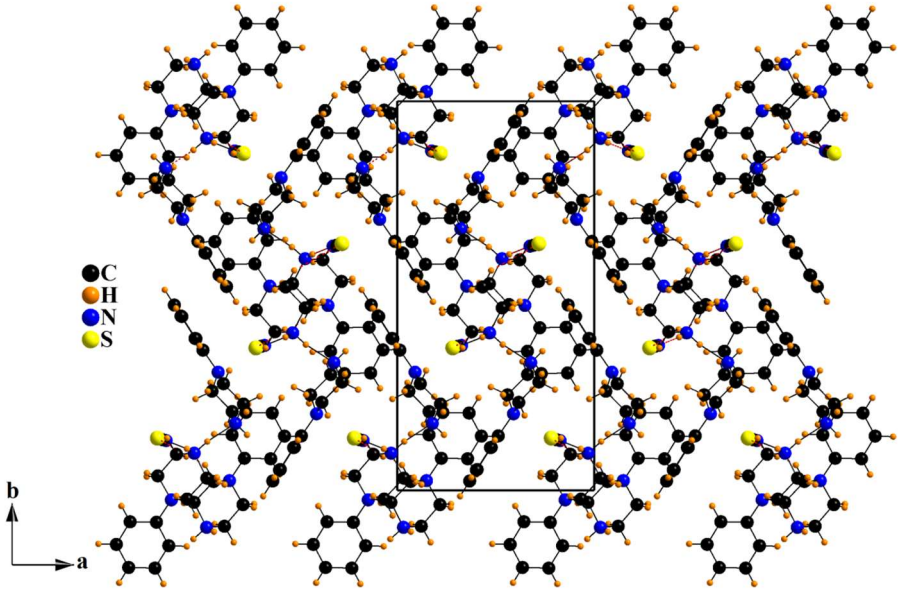

Fig. 6: Projection of the structure of (II) along the *c*-axis.

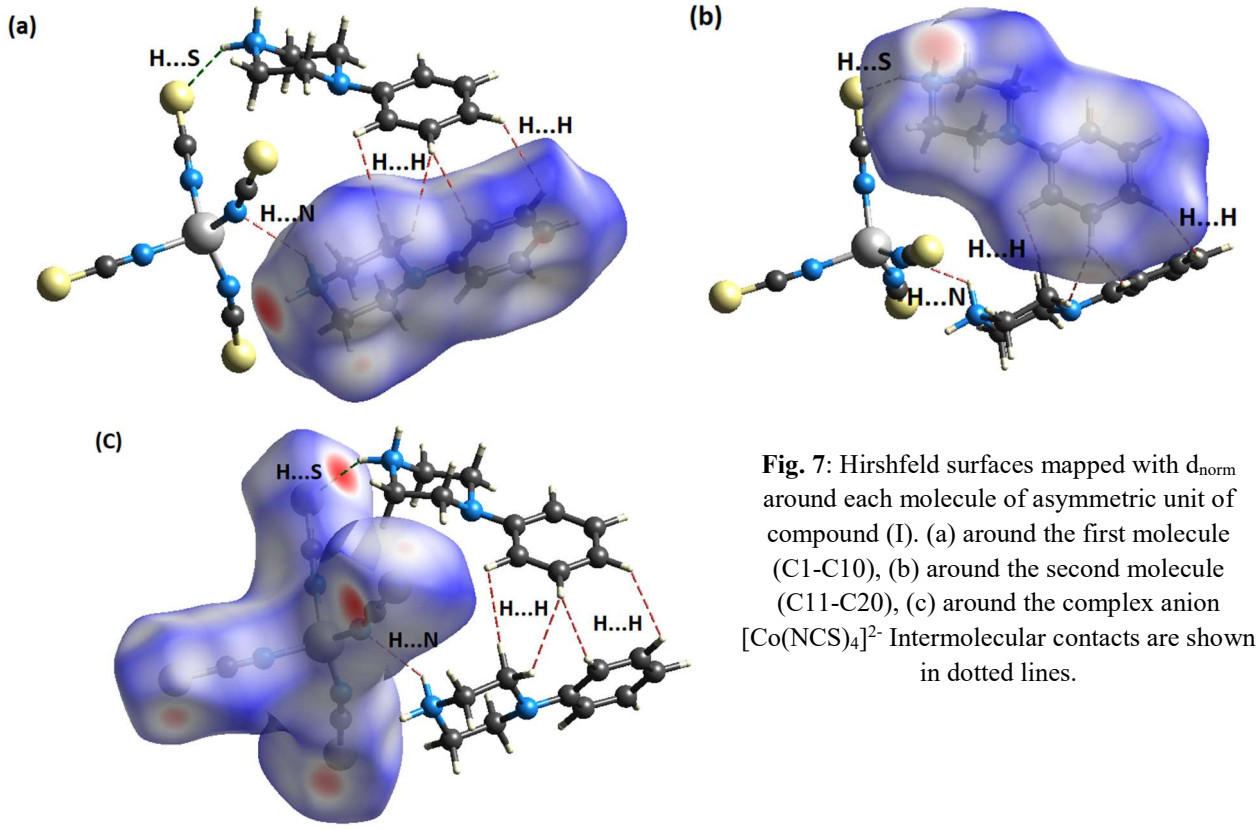

Fig. 7: Hirshfeld surfaces mapped with d_{norm} around each molecule of asymmetric unit of compound (I). (a) around the first molecule (C1-C10), (b) around the second molecule (C11-C20), (c) around the complex anion $[Co(NCS)_4]^{2-}$ Intermolecular contacts are shown in dotted lines.

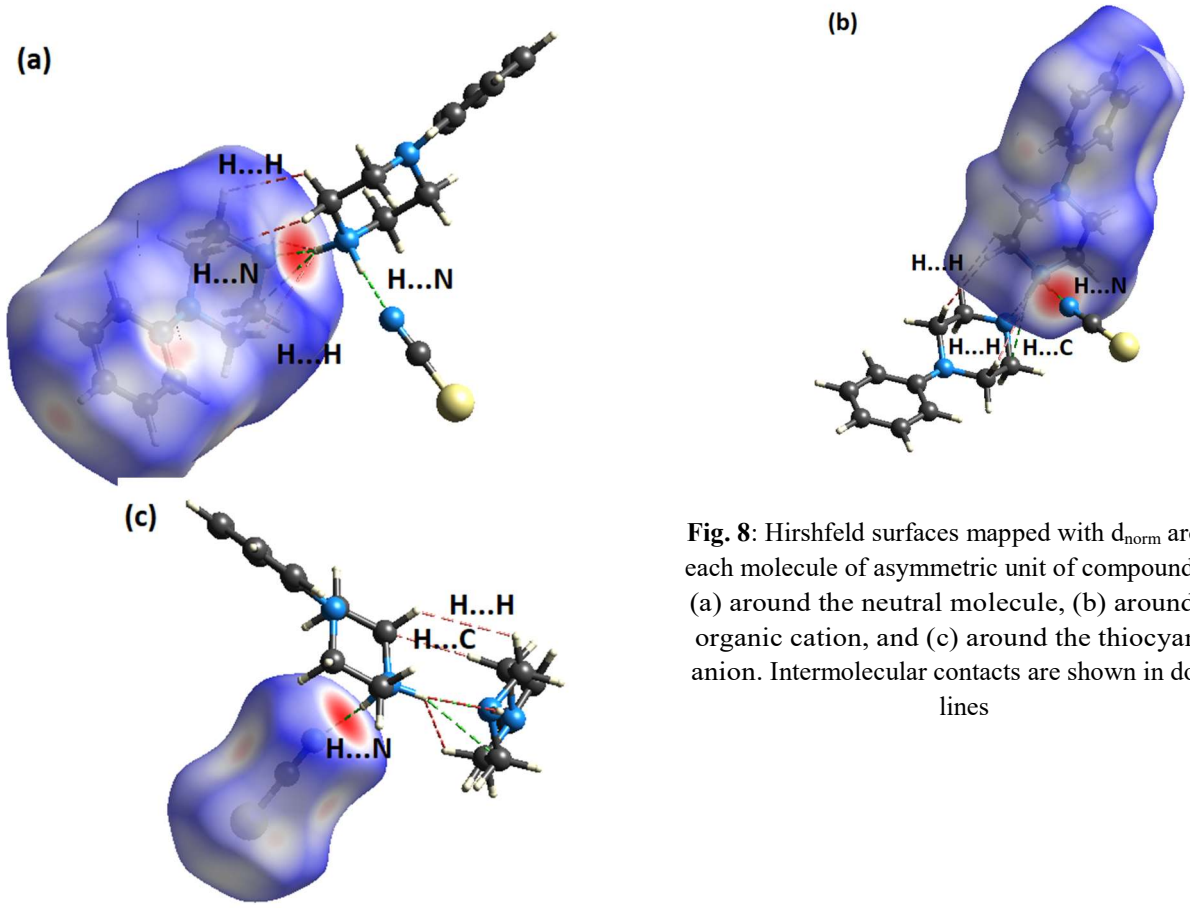

Fig. 8: Hirshfeld surfaces mapped with d_{norm} around each molecule of asymmetric unit of compound (II). (a) around the neutral molecule, (b) around the organic cation, and (c) around the thiocyanate anion. Intermolecular contacts are shown in dotted lines

A)

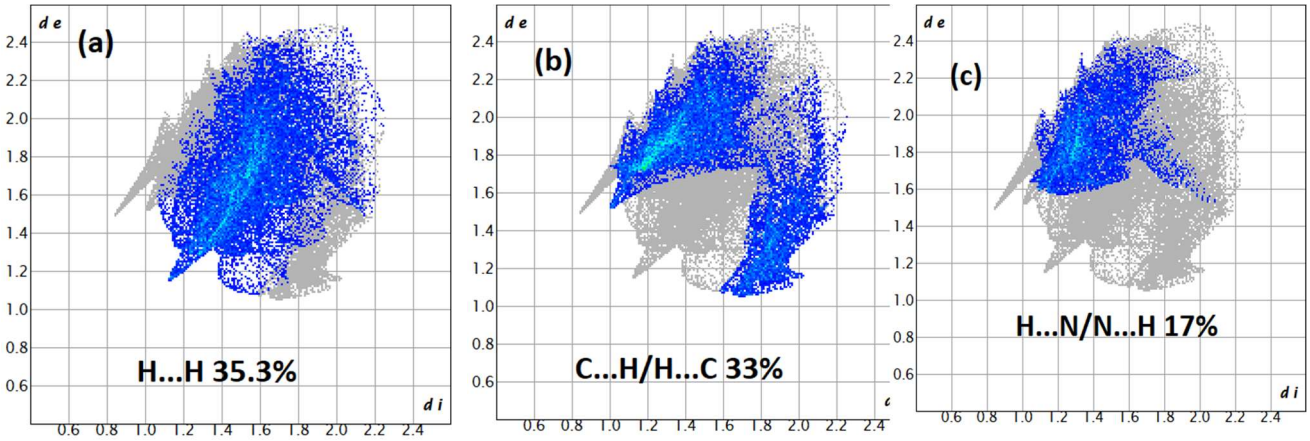

B)

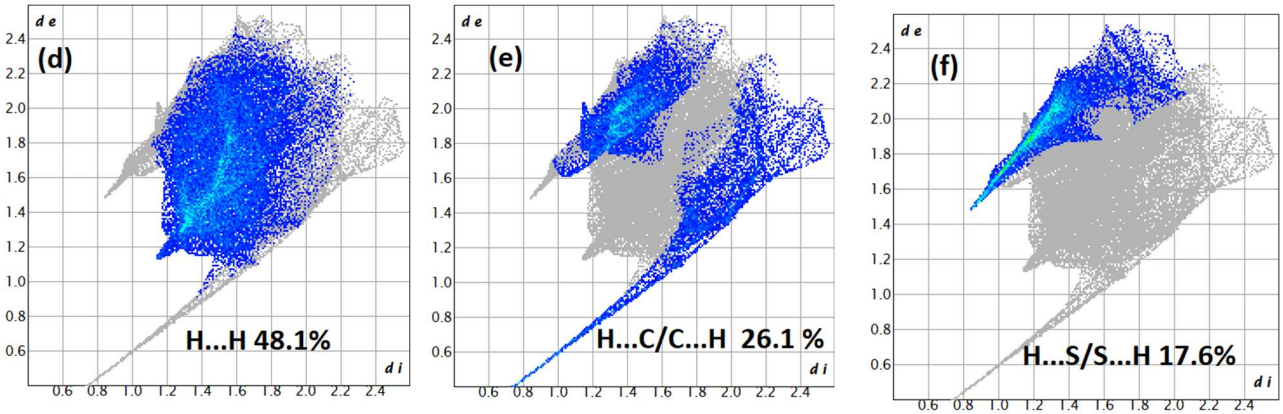

C)

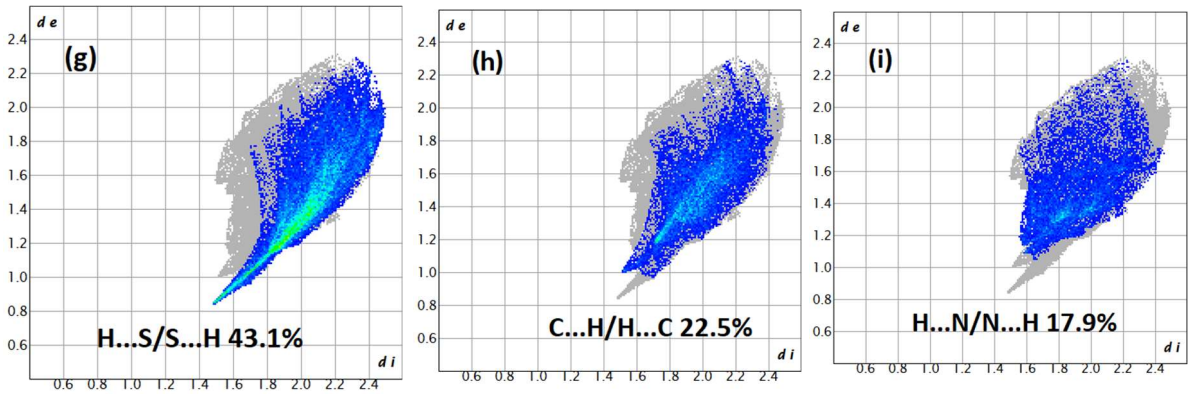

Fig.9. 2D Fingerprint plots of each molecule in asymmetric unit in compound (I). (**A**) for the first molecule (C1-C10). (**B**) for the second molecule (C11-C20). (**C**) for the inorganic anion $[Co(NCS)_4]^{2-}$

(a)

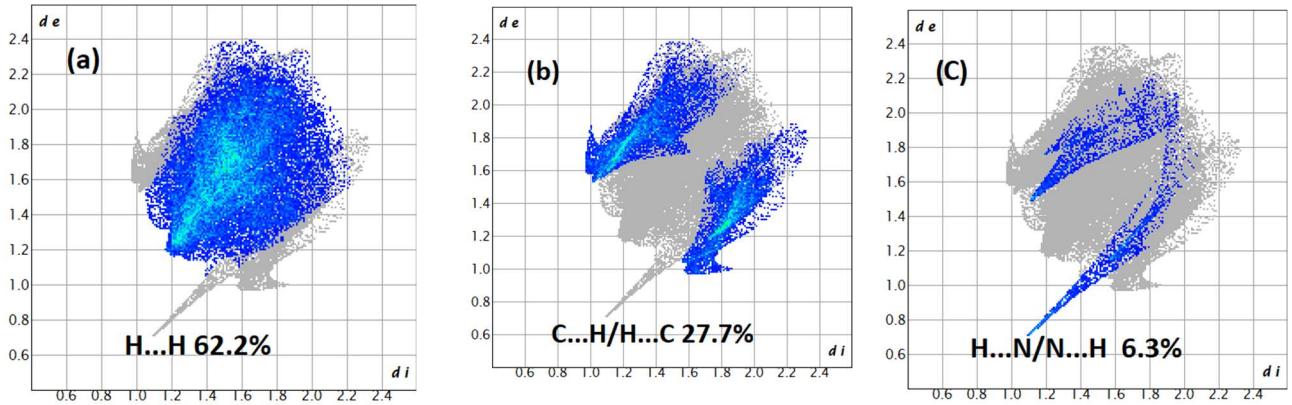

(B)

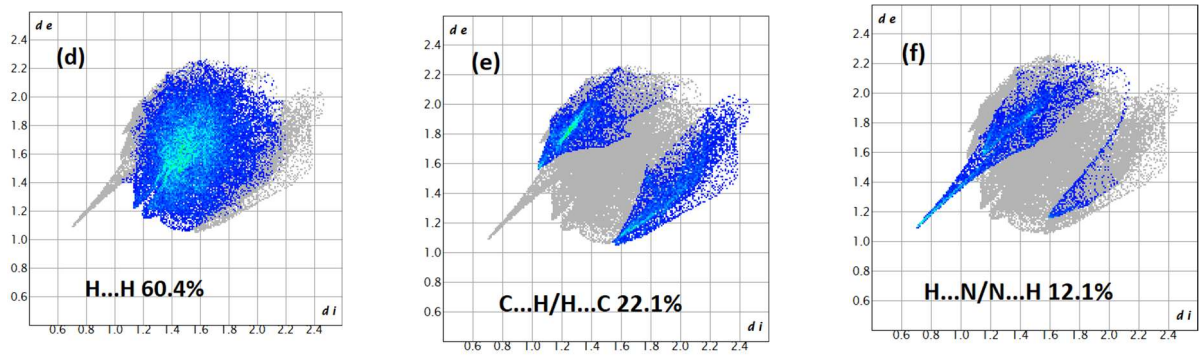

(C)

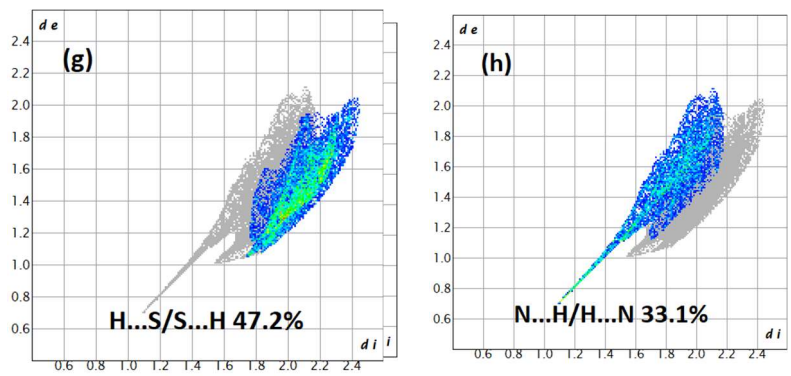

Fig.10. 2D Fingerprint plots of each molecule of asymmetric unit in compound (II). (**A**) for the first molecule (C1-C10). (**B**) for the second molecule (C11-C20). (**C**) for the NCS^{-} anion..

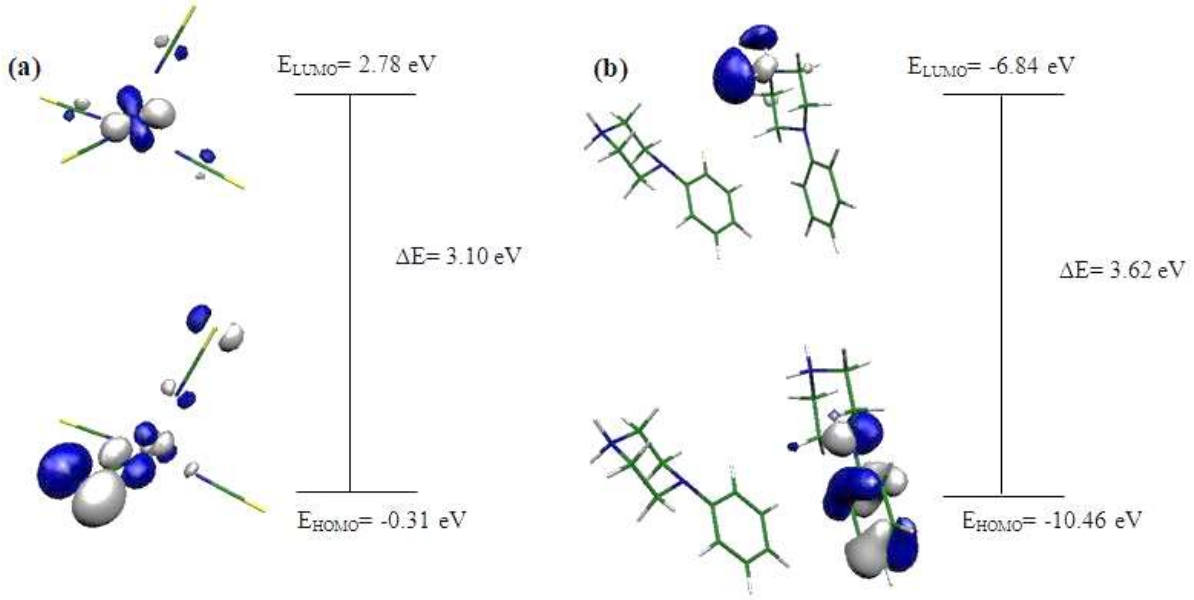

Fig. 11: Frontier orbitals of the anionic complex (a) and organic cations (b) of (I).

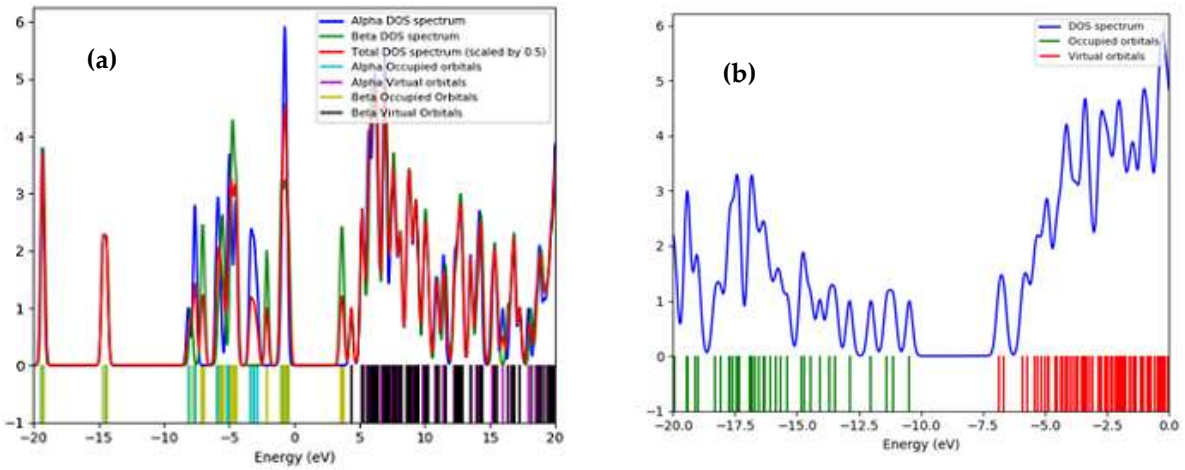

Fig. 12: Energy distribution of the different orbitals for (I). (a) around the $Co(NCS)_4$ entity,

(b) around the organic entity

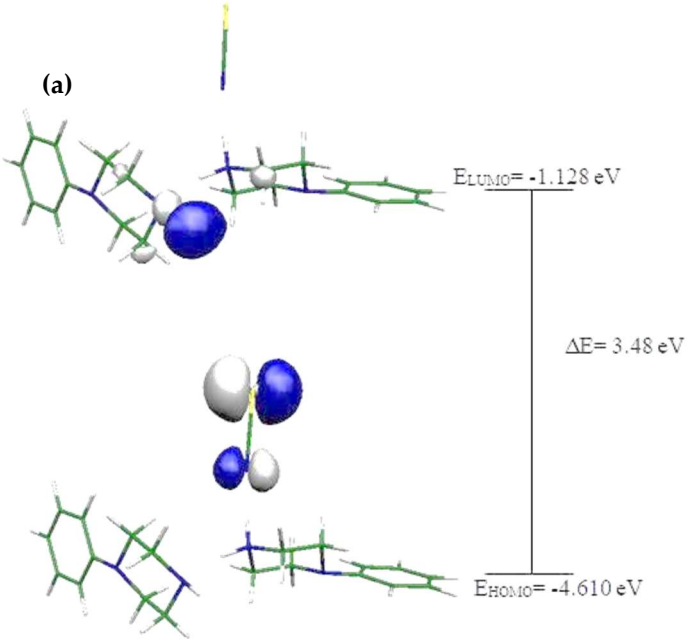

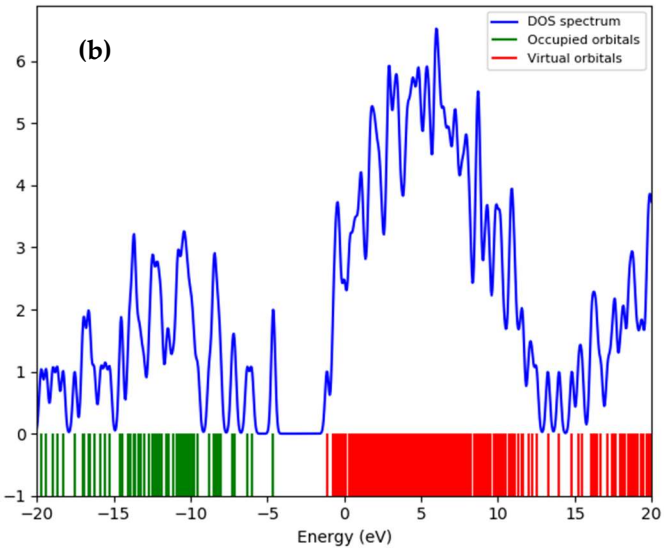

Fig.13: (a) Frontier orbitals and (b) energy distribution of the different orbitals for (II).

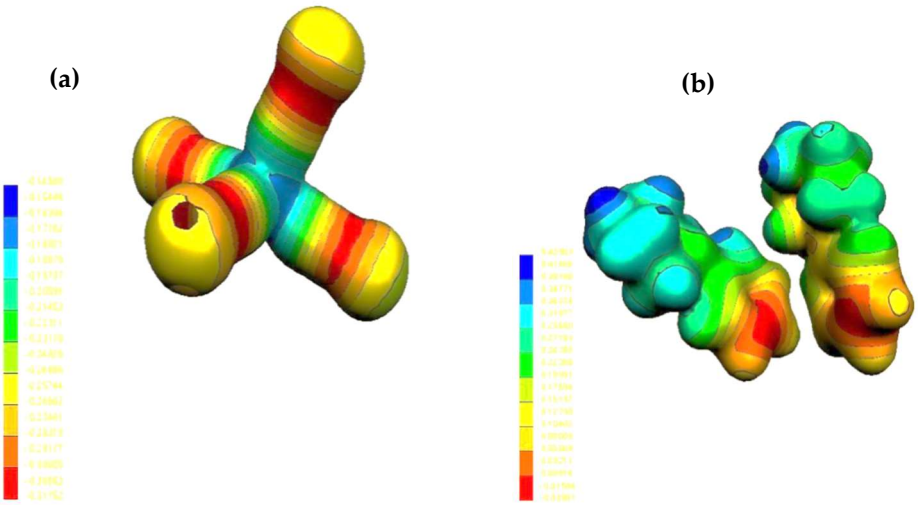

Fig. 14. MEP surfaces of compound (I). (a) around the thiocyanate anion, (b) around the organic cations.

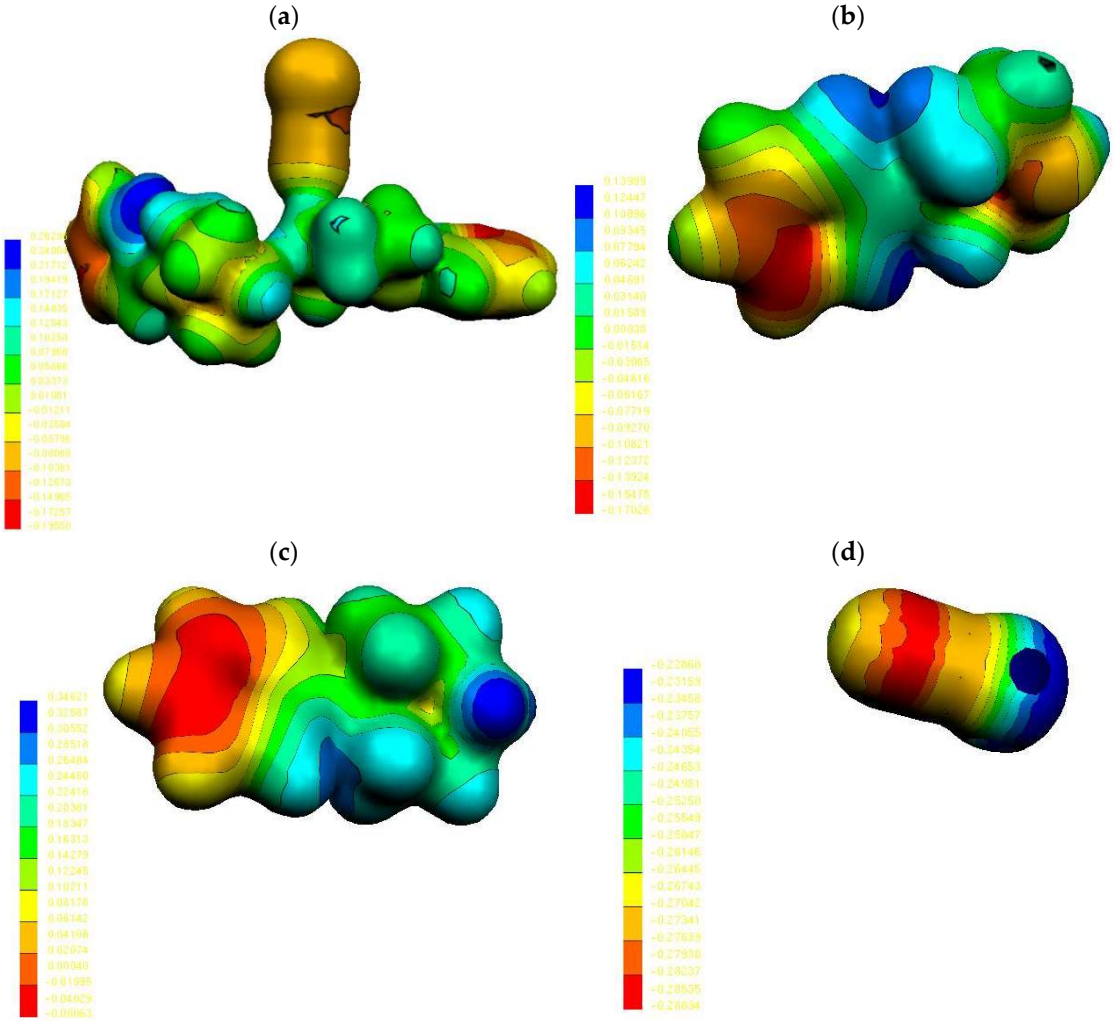

Fig. 15: MEP surfaces of compound (II). (a) around the complex system, (b) around the neutral molecule, (c) around the organic cation, and (d) around the thiocyanate anion.

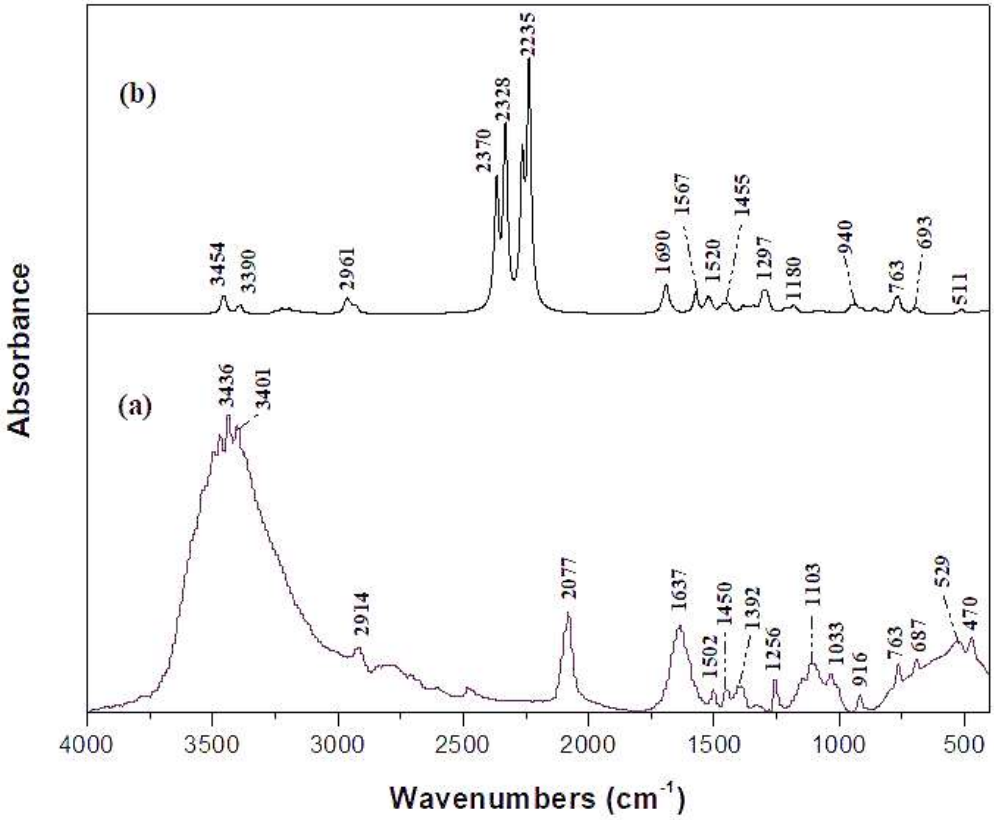

Fig. 16: Experimental (a) and calculated (b) IR spectra of (I).

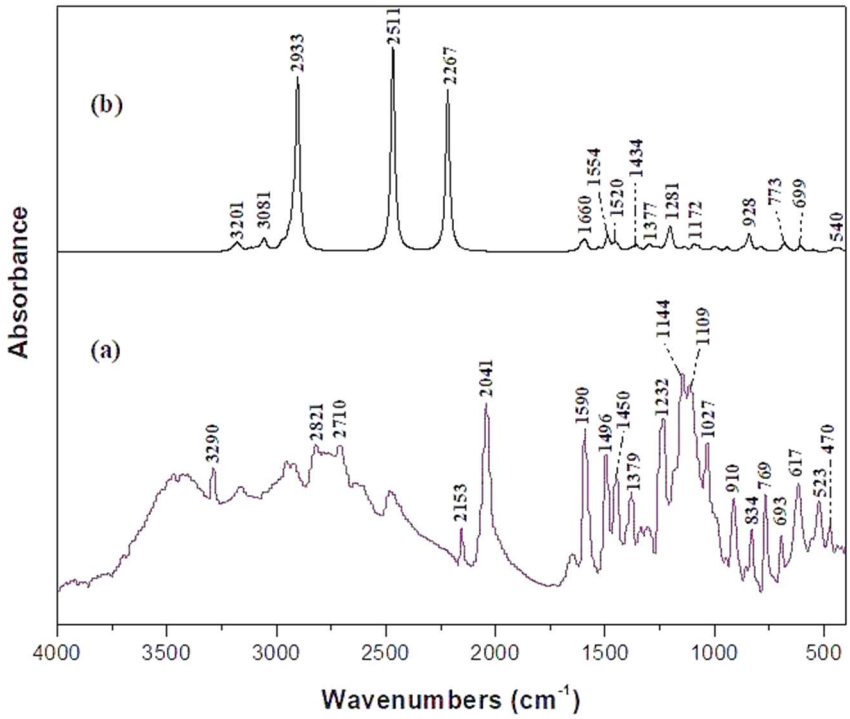

Fig. 17: Experimental (a) and calculated (b) IR spectra of (II).

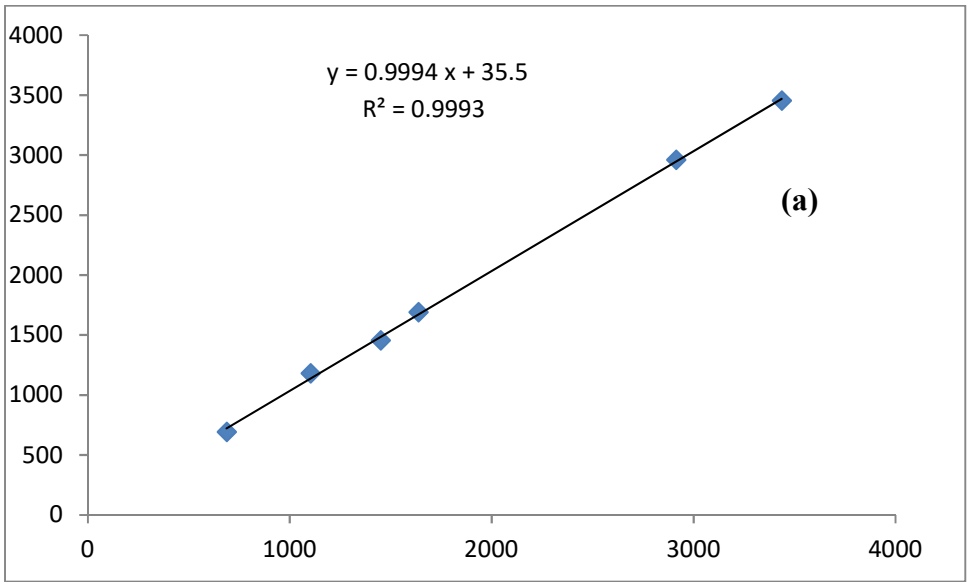

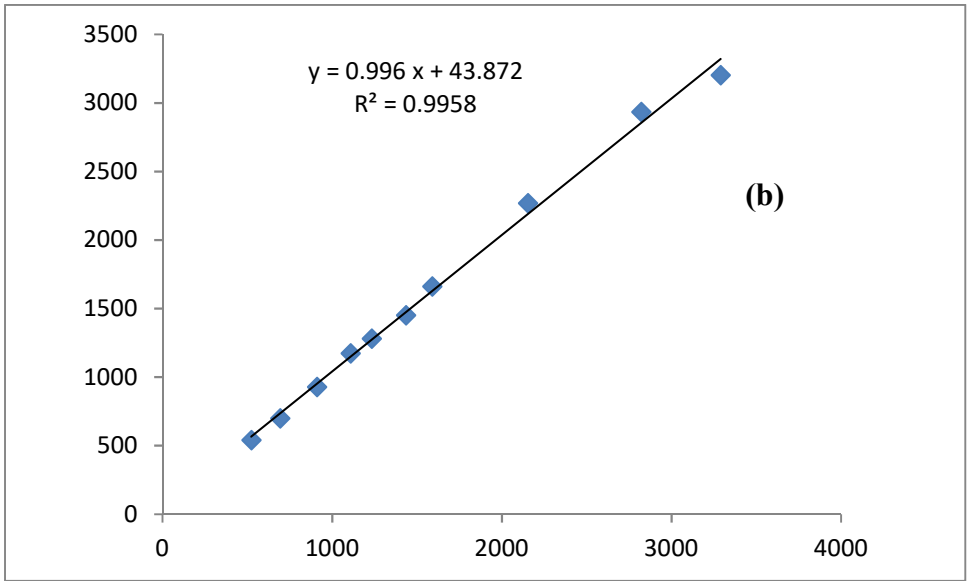

Fig. 18: Comparison between experimental and calculated IR frequencies of (a) (I) and (b) (II).

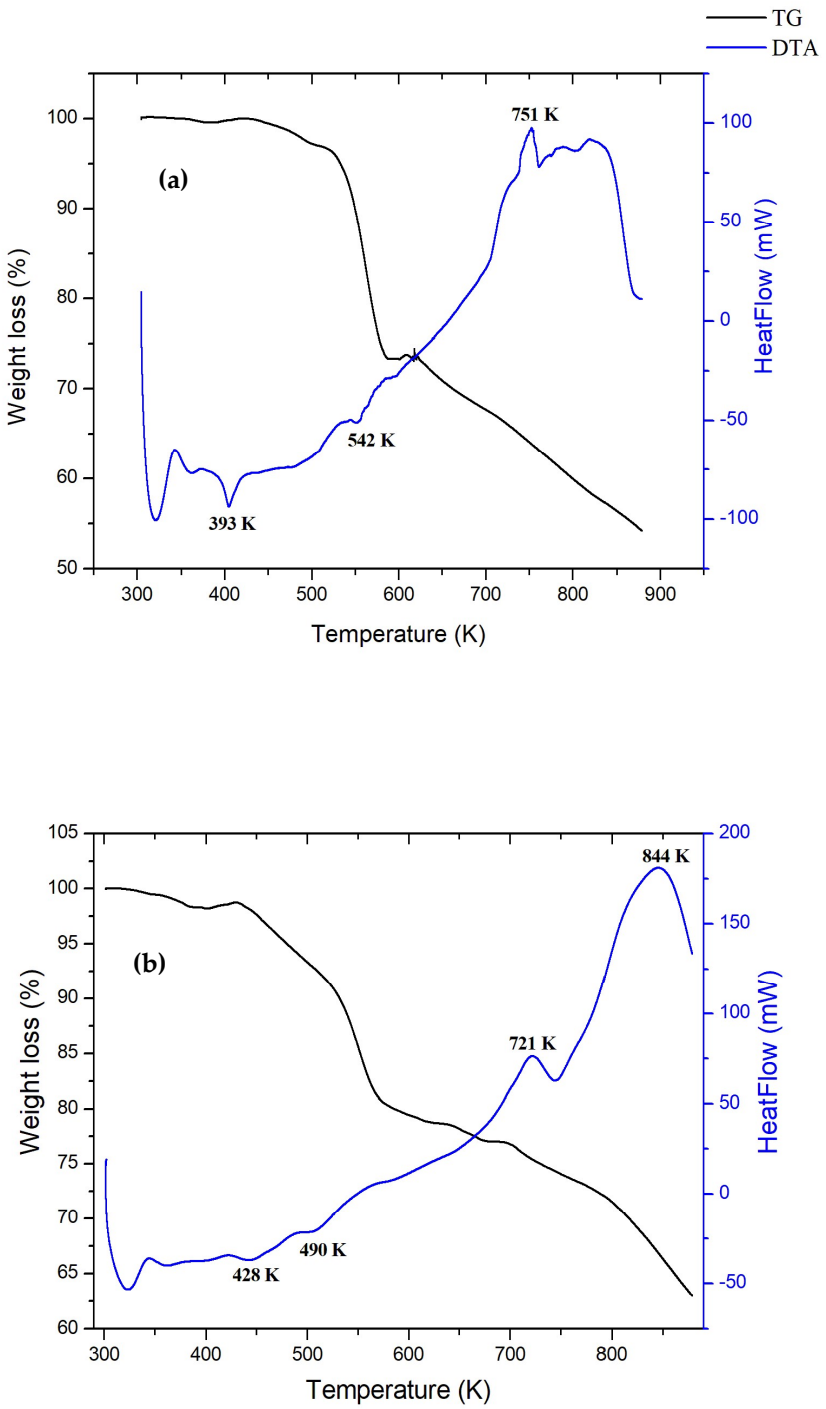

Fig. 19: Simultaneous curves of thermogravimetric analysis and differential thermal analysis of (a) (I) and (b) (II).

Table-1: Crystallographic data and structure refinement for the crystals**.**

Acronym Formula	$(HPhPip)_2[Co(NCS)_4]$ (I)	(HPhPip)(NCS)·PhPip (II)
Formula weight (g mol^{-1})	617.73	383.55
Crystal system	Triclinic	Orthorhombic
Space group	$P\bar{1}$	$Pna2_1$
Crystal size (mm)	0.15 × 0.10 × 0.05	0.55 × 0.46 × 0.25
Radiation, wavelength (Å)	Mo*K*α, 0.71073	Mo*K*α, 0.71073
Unit-cell dimensions: *a*, *b*, *c* (Å)	10.5582(11), 11.6606(13), 12.9724(14)	10.4089(2), 20.5701(4), 9.4259(2)
α, β, γ (°)	105.312(7), 112.603(6), 92.948(7)	
V ($Å^3$)	1401.0(3)	2018.20(7)
Z	2	4
Density calc. (g cm^{-3})	1.464	1.262
Absorption coefficient μ (mm^{-1})	0.941	0.176
Crystal temperature (K)	100(2) K	100(2) K
Diffractometer	Bruker APEX II	Nonius Kappa CCD
F(000)	642	824
θ-range for cell determination (°)	1.787–26.420	2.193–28.288
Limiting indices: ±h, k, l	$-13 \leq h \leq 13$. $-14 \leq k \leq 14$	$-12 \leq h \leq 12$. $-13 \leq k \leq 13$
	$-16 \leq l \leq 16$	$-27 \leq l \leq 27$
Refinement method	Full matrix least-squares on F^2	Full matrix least squares on F^2
Reflections collected/unique: R_{int}	56091 / 5725 (R_{int} = 0.1412)	101443 / 4829 (R_{int} = 0.058)
parameters	334	257
R indices (all data, on F^2), Esd	R = 0.046, Rw = 0.0759, S = 1.031	R = 0.0413, Rw = 0.0904, S = 1.054
Δ_ρ(min, max) (e $Å^{-3}$)	$-0.540 < \Delta\rho < 0.629$	$-0.186 < \Delta\rho < 0.366$
CCDC N°	2072863	2072865

Table 2: Selected bond lengths and angles (Å, °) of (I) and (II).

Distances (Å)		**Angles (°)**	
(I)			
Co1—N5	1.961(4)	N5—C21—S1	179.1(4)
Co1—N6	1.961(4)	N6—C22—S2	178.7(4)
Co1—N7	1.972(4)	N7 —C23—S3	179.1(4)
Co1—N8	1.952(3)	N8—C24—S4	179.9(4)
N5—C21	1.154(5)	C21—N5—Co1	176.0(4)
N6—C22	1.172(5)	C22—N6—Co1	160.0(3)
N7—C23	1.158(5)	C23—N7—Co1	172.5(3)
N8—C24	1.169(5)	C24—N8—Co1	161.5(3)
C21—S1	1.634(5)	N8—Co1—N5	109.66(15)
C22—S2	1.628(4)	N8—Co1—N6	117.04(14)
C23—S3	1.642(5)	N5—Co1—N6	102.24(15)
C24—S4	1.627(4)	N8—Co1—N7	107.48(15)
		N5—Co1—N7	104.13(15)
		N6—Co1—N7	115.31(14)
(II)			
C21—S1	1.644(2)	N5—C21—S1	179.3(2)
N5—C21	1.164(3)	C2—C1—C6	117.77 (17)
C1—C2	1.400 (3)	C2—C1—N1	120.53 (19)
C1—C6	1.412 (3)	C6—C1—N1	121.66 (19)
C1—N1	1.416 (2)	C3—C2—C1	120.7 (2)
C2—C3	1.393 (3)	C4—C3—C2	121.1 (2)
C3—C4	1.389 (3)	C5—C4—C3	118.91 (18)
C4—C5	1.380 (3)	C4—C5—C6	120.9 (2)
C5—C6	1.400 (3)	C5—C6—C1	120.6 (2)
C7—N1	1.472 (3)	N1—C7—C8	110.67 (17)
C7—C8	1.516 (3)	N2—C8—C7	110.01 (16)
C8—N2	1.473 (3)	N2—C9—C10	109.90 (17)
C9—N2	1.470 (3)	N1—C10—C9	111.35 (16)
C9—C10	1.518 (3)	C16—C11—C12	118.72 (18)
C10—N1	1.472 (3)	C16—C11—N3	122.76 (17)
C11—C16	1.395 (3)	C12—C11—N3	118.52 (16)
C11—C12	1.402 (3)	C13—C12—C11	120.56 (19)
C11—N3	1.424 (2)	C12—C13—C14	120.38 (19)
C12—C13	1.392 (3)	N3—C20—C19	110.58 (17)
C13—C14	1.393 (3)	C1—N1—C7	116.83 (16)
C14—C15	1.382 (3)	C1—N1—C10	115.76 (16)
C15—C16	1.403 (3)	C7—N1—C10	112.39 (15)
C17—N3	1.463 (2)	C9—N2—C8	109.08 (16)
C17—C18	1.517 (3)	C11—N3—C17	116.23 (15)
C18—N4	1.489 (3)	C11—N3—C20	113.29 (15)
C19—N4	1.499 (2)	C17—N3—C20	109.36 (16)
C19—C20	1.519 (3)	C18—N4—C19	111.54 (16)
C20—N3	1.475 (3)		

Table-3: Hydrogen-bond geometry (Å, °) of (I) and (II).

D—H…A	**D—H (Å)**	**H…A (Å)**	**D…A (Å)**	**D—H…A (°)**
(I): Symmetry codes: (i) x, y − 1, z ; (ii) −x + 1, −y + 2, −z + 1 ; (iii) −x, −y + 2, −z + 1.				
C(12)-H(12)...S(2) [i]	0.95	2.73	3.643(4)	162.7
N(2)-H(2A)...S(4) [ii]	0.91	2.45	3.353(4)	174.3
N(2)-H(2B)...S(2) [iii]	0.91	2.46	3.348(4)	166.8
N(4)-H(4A)...S(3)	0.91	2.50	3.295(3)	146.4
N(4)-H(4B)...S(1) [i]	0.91	2.44	3.317(4)	161.8
(II): Symmetry codes: (i) x, y, z − 1; (ii) −x + 1, −y + 1, z − 1/2.				
C(18)-H(18B)...S(1) [i]	0.99	2.98	3.466(2)	111.5
C(20)-H(20B)...S(1) [ii]	0.99	2.89	3.7525(19)	145.7
N(4)-H(2M)...N(5)	0.81(3)	2.00(3)	2.816(3)	174(3)
N(4)-H(2N)...N(2)	0.95(3)	1.88(3)	2.825(3)	168(2)

Table 4. Statistical analysis of intermolecular contacts. The Hirshfeld surface was computed around each molecule of the asymmetric unit of compound (**I**). The second row shows the chemical content on the Hirshfeld surface. The third row and the upper/right part of the last five lines show the % *C*xy of the contact types on the surface. The lower/left part of the last five lines is in italics and shows the *E*xy enrichment ratios of contact types. The major *C*xy contact and the significantly enriched contacts (E_{XY} >> 1) are in bold. (**a**) around the first molecule C1–C10. (**b**) around the second molecule C11–C20. (**c**) around the inorganic anion.

(**a**)					
atom	H	C	N	S	Co
% Surface	**66.5**	**17.7**	9.55	6.15	0
% self contact	35.3	0.5	0.4	0	0
H	*0.79*	33	17	**12.2**	0.2
C	***1.40***	*0.15*	1.3	0.1	0
N	***1.33***	*0.38*	*0.43*	0	0
S	***1.49***	*0.04*	*0*	*0*	0
Co	***1.50***	*0*	***0***	*0*	*0*
(**b**)					
atom	H	C	N	S	Co
% surface	**71.75**	**15.05**	2.25	10.95	0
% self contact	**48.1**	0.3	0	0	0
H	*0.93*	**26.1**	3.6	**17.6**	0
C	***1.20***	*0.13*	0	3.4	0
N	***1.11***	*0.38*	*0*	0.9	0
S	***1.20***	*0.04*	*0*	*0*	0
Co	*0*	*0*	***0***	*0*	*0*
(**c**)					
atom	H	C	N	S	Co
% surface	**41.85**	**14.7**	13.55	29.05	0.75
% self contact	**0**	0.3	0	1.3	0
H	*0*	**22.5**	17.9	**43.1**	0.2
C	***1.83***	*0.13*	2,2	4.1	0
N	*1.57*	*0.55*	*0*	7	0
S	***1.77***	*0.48*	*0.88*	*0.15*	1.3
Co	*0.31*	*0*	***0***	***2.98***	*0*

Table 5. Statistical analysis of intermolecular contacts. The Hirshfeld surface was computed around each molecule of the asymmetric unit of compound II. (**a**) around the first molecule C1-C10. (**b**) around the second molecule C11-C20. (**c**) around the inorganic anion. Mulliken charge distribution in the $[Co(NCS)_4]^{2-}$ anion in $(HPhPip)_2[Co(NCS)_4]$ (I).

(**a**)				
atom	H	C	N	S
% Surface	**81.1**	**13.85**	3.15	1.9
contacts	**H...H**	C...H	N...H	H...S
% Contacts	**62.2**	27.7	6.3	3.8
Enrichment	0.94	**1.23**	1.24	**1.23**
(**b**)				
atom	H	C	N	S
% Surface	**80.2**	**11.05**	6.05	2.7
contacts	**H...H**	C...H	N...H	H...S
% Contacts	**60.4**	22.1	12.1	5.4
Enrichment	0.93	**1.24**	1.24	**1.24**
(**c**)				
atom	H	C	N	S
% Surface	**49.95**	**9.8**	16.6	23.65
contacts	**N...S**	C...H	N...H	H...S
% Contacts	**0.1**	19.6	33.1	47.2
Enrichment	0.012	**2.00**	1.99	**1.99**
Atom				
Co	0.122102			
N	0.125364	−0.100738	0.065526	−0.072062
C	−0.153321	−0.123837	−0.154720	−0.128370
S	−0.425894	−0.369055	−0.408583	−0.376412

Table 6: Mulliken charge distribution in the organic cations of $(HPhPip)_2$ $Co(NCS)_4$ (I).

Atom	Cation 1		Cation 2	
N1	-0.058774		-0.102222	
N4	-0.797766		-0.875198	
H(N4)	0.515537 0.488588		0.514009 0.515426	
C2-C6	-0.705337	-0.270850	-0.275462	-0.295483
H(C2-C6)	0.244199 0.243613	0.256093 0.230764	0.244930 0.238648	0.253566 0.246958
C3-C5	-0.313992	-0.278018	-0.147616	-0.196395
H(C3-C5)	0.290096 0.255935	0.267876 0.285510	0.259658 0.269822	0.273608 0.273183
C7	-0.559301		0.003248	
C8-C12	0.452388	0.796372	0.127485	0.523031
H(C8-C12)	0.164666	0.135026	0.182381	0.140047
C9-C11	-0.927546	-0.292636	-0.915376	-0.690372
H(C9-C11)	0.205113	0.186380	0.210799	0.183143
C10	-0.077135		-0.105465	
H(C10)	0.204479		0.202366	

Table 7: Mulliken charge distribution in and (HPhPip)(NCS)·PhPip (II).

Atom	Cation		Neutral molecule	
N1	-0.096398		-0.126888	
N4	-0.825551		-0.694078	
H(N4)	0.540931 0.583385		0.425933	
C2-C6	-0.540137	-0.494353	-0.038437	-0.097639
H(C2-C6)	0.218426 0.266010	0.264822 0.215847	0.212566 0.237571	0.200216 0.200512
C3-C5	-0.287417	-0.128941	-0.631687	-0.570925
H(C3-C5)	0.241799 0.231310	0.226946 0.242197	0.222381 0.216762	0.217325 0.207032
C7	0.036515		-0.042249	
C8-C12	-0.179061	0.238141	0.142043	0.952657
H(C8-C12)	0.167801	0.178907	0.158673	0.178056
C9-C11	-0.350098	-0.341968	-0.792576	-1.006672
H(C9-C11)	0.180451	0.183701	0.176544	0.185209
C10	-0.171483		-0.075151	
H(C10)	0.179729		0.177509	
Anion				
N	-0.436610			
C	-0.090447			
S	-0.289139			

Table 8: Test results of the tested compounds (I) and (II) for the bacterial activity.

	Inhibition zone diameter (mm)			
	Escherichia coli	**Salmonella typhimurium**	**Candida albicans**	**Enterococcus feacium**
Ampicilline/ Nystatine (10µg/100µg)	11.75±0.3	13.75±1.0	19.83±0.2	26.5±0.7
Compound (I)	11.5±0.7	10±0.0	14.5±0.7	12.75±0.3
Compound (II)	8.75±1.0	7.75±1.0	10±0.0	6.5±0.0
	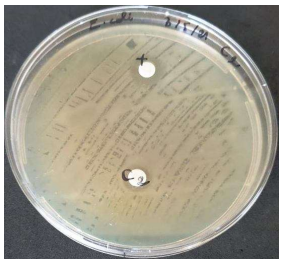	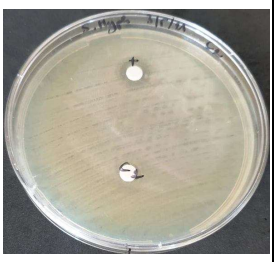		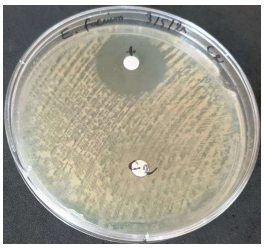

Table 9: Antifungal and antibacterial activities of metal complexes.

	Inhibition Zone Diameter (mm/mg Sample)			
	Gram-Negative Bacteria		**Gram-Positive Bacteria**	**Fungi**
	Escherchia coli	*Salmonella typhimurium*	*Enterococcus feacium*	*Candida albicans*
$Co(NCS)_4(C_{10}H_{15}N_2)_2$ (I)	11.5 ± 0.7	10 ± 0.0	12.75 ± 0.3	14.5 ± 0.7
$C_{21}H_{29}N_5S$ (II)	8.75 ± 1.0	7.75 ± 1.0	6.5 ± 0.0	10 ± 0.0
$Co(NCS)_4$ $(C_8H_{14}N_4).H_2O$ [74]	9 ± 0.0	10.5 ± 0.7	10.75 ± 0.3	11.5 ± 0.7